Novel synthesis and characterization of SiO_2 nanopowders doped with Sr^{2+} and co-doped with Tb^{3+} dispersed in PLA for application in light emitting material.

by

Rantooa Goodchild Moji

BSc (Hons), MA (HES)

Submitted in accordance with the requirements for the degree

MAGISTER SCIENTIAE (MSc) IN POLYMER SCIENCE

FACULTY OF NATURAL AND AGRICULTURAL SCIENCE

DEPARTMENT OF CHEMISTRY

at the

UNIVERSITY OF THE FREE STATE (QWAQWA CAMPUS)

SUPERVISOR: PROF L.F. KOAO

CO-SUPERVISORS: DR J.P. MOFOKENG

: PROF S.V. MOTLOUNG

November 2020

Declaration

"I declare that the thesis hereby submitted by me for the MSc degree at the University of the Free State is my own independent work and has not previously been submitted by me at another university/faculty. I furthermore, cede copyright of the thesis in favour of the University of the Free State."

Moji RG (Mr)

Dedication

To my departed role models and motivators SOM and Ntsu Moji you have set me very high standards and I hope not to disappoint.

Acknowledgements

“For I know the plans I have for you,” declares the LORD, “plans to prosper you and not to harm you, plans to give you hope and a future” (Jer. 29:11)

To the two most beautiful women in my life, the queen of my castle Titi Moji and the queen mother Bernice Moji I can’t thank you enough for the encouragement and support throughout the project.

To my supervisor Prof. L.F. (Thami) Koao and co-supervisor Dr. J.P. Mofokeng my gratitude for believing that I still had it in me to see this project through.

The members of Prof. Koao’s research group Hille and Mipi I will be forever grateful for your inputs and assistance.

To my colleagues and comrades at the Qwaqwa campus of the University of the Free State, especially in the Chemistry department you guys rock!

To Prof. S.V. Motloung for your unwavering support and those random calls to nudge in the right direction.

Dr. James Wesley-Smith at Electron Microscopy Unit at Sefako Makgatho Health Science University is also acknowledged for the SEM and TEM images.

Prof. Kroon and your students for assistance with the UV, PL and XRD analysis.

This work is supported financially by the South African National Research Foundation (NRF) Thuthuka Programme (fund number: UID 99224), NRF incentive funding for rated researchers (IPRR) (Grant No: 126914) and the University of the Free State.

Abstract

The immobilization of the phosphor particles in a polymer matrix helps to overcome the problem of emitter layer thickness and thus the reproducibility of the emitted light experienced when phosphors are immobilized in glues such as polyurethane or epoxy resin. In this study composites of SiO_2:0.4 mol% Sr^{2+}:x mol% Tb^{3+} (with x = 0.02, 0.06, 0.1, 0.3, 0.4, 0.5) nano-powders dispersed in PLA polymer matrix were successfully prepared through melt mixing. The challenge as shown by the TEM images is that the filler particles tend to agglomerate in the polymer matrix. The XRD results showed broad peaks for all samples, which meant the samples were amorphous. The introduction of the nano-powders into the polymer matrix did not result in the change in the morphology of the samples. The emission peaks that can be associated with the Tb^{3+} transitions were observed with the dispersion of the nano-powders into the PLA.

The SiO_2 based phosphors used in this study were prepared using the sol-gel technique and characterized by SEM, TEM, XRD, UV and PL. The SiO_2 doped with Sr^{2+} samples showed an increase in crystallinity with increasing Sr^{2+} concentration. These singly doped samples showed the highest luminescence at 0.4 mol% Sr^{2+} concentration, and the CIE analysis showed that the colour coordinates of SiO_2:0.4 mol% Sr^{2+} were related to white light emission. This SiO_2:0.4 mol% Sr^{2+} sample that showed the highest luminescence was co-doped with different mol% Tb^{3+}. The co-doped samples were found to be amorphous with the co-doping and not having any significance on the shape of the particles. The addition of Tb^{3+} tuned the colour of the phosphors from blue to green.

Key words: PLA, SiO_2, Terbium, Strontium, Photoluminescence, Morphology, CIE.

LIST OF ABBREVIATIONS

CIE	Commission Internationale de l'Eclairage
DSC	Differential scanning calorimetry
DTG	Derivative Thermogravimetric
PLA	Poly lactic acid
PL	Photoluminescence
RE	Rare earth
SEM	Scanning electron microscope
TEM	Transmission electron microscope
TGA	Thermogravimetric analysis
XRD	X-ray diffraction
UV	Ultraviolet spectroscopy

TABLE OF CONTENTS

List of Figures

List of Tables

Chapter 1 – Background and Objectives

1.1 Background

Phosphors have been studied for over a century [1], but due to technological advances, there is still a need to devote time to study them. In recent times white light emitting diodes (w-LED) have attracted a lot of attention due to their favorable characteristics such as long lifetime, low energy consumption, higher reliability and environment-friendly affiliation [2]. The disadvantages with the LED's is that they degrade with time, which means they will have short life span. By incorporating or dispersing the phosphors in polymers, we will be improving their life span. Luminescent glasses have been found to be promising phosphor candidates for w-LED's as compared to conventional phosphors [3]. Thus, this study envisages to produce phosphors from silica (SiO_2) based glass that is doped with Sr^{2+} and co-doped with Tb^{3+}, and then disperse these SiO_2: Sr^{2+}: Tb^{3+} nano-particles with various compositions in Polylactic acid (PLA). This dispersion in PLA it is envisaged that it will help overcome luminescence quenching mechanisms that rare earth doped sol-gel glasses are susceptible to and improve the life span of light emitting materials (e.g. LED'S).

Sol-gel silica (SiO_2) has been widely used as a host material for lanthanide ions because it has good physical properties and chemical stability [4]. The sol–gel process, which consists of two steps, namely, hydrolysis of a metal alkoxide and polycondensation of the hydrolysis products is the preferred method to prepare SiO_2 particles [5]. This process involves the synthesis of an inorganic and/ or organic network by a chemical reaction in solution at low (generally ambient) temperatures followed by the transition from solution to colloidal sol and to a multiphasic gel form. According to the different precursors utilized, the sol-gel techniques can be divided into three types: (1) the sol-gel route based upon hydrolysis-condensation of metal-alkoxides; (2)

the gelation route based upon concentration of aqueous solutions involving metal-chelates, often called as “chelate gel” route; and (3) the polymerizable-complex (PC) route [6]. Apart from the tetraethyl orthosilicate (silicon alkoxide), most of the metal alkoxides suffer from high cost, unavailability, toxicity, and fast hydrolysis rate (thus difficult in controlling the homogeneity of different components during experimental processes) [7]. Microporous silica prepared by the sol-gel technique is considered an optically inert medium and its chemical and thermal stability increase its attractiveness as a host for luminescent ions [8]. Further advantages of the sol-gel process are that it can produce very pure glass at temperatures well below the melting point, and it allows incorporation of much higher concentration of dopants than the melt process [9 – 12].

Tb^{3+} ions are used as the activator because their bright green emission is suitable for many applications. The challenge with the use of Tb^{3+} ions is that they show strong absorption in the range 240 -260 nm, which is difficult to access [4, 13]. Co-doping with sensitizer ions that have transitions at more accessible and convenient wavelengths enhances the luminescence efficiency of Tb^{3+} ions. Several studies have found that Ce^{3+} ions are an efficient sensitizer for Tb^{3+} [14 - 20]. The energy transfer from the sensitizer ions to activator ions play an important role of enhancing the luminescence efficiency of phosphor materials [21].

On the other hand, PLA is a linear aliphatic thermoplastic polyester, which has obtained much attention because of its excellent biodegradability, compatibility and high strength and it comes from renewable sources [22, 23]. PLA offers a possible alternative to the traditional non-biodegradable polymers such as polyethylene and polypropylene especially when recycling them is difficult or not economical. However, some of its disadvantages, such as relatively poor mechanical properties and gas barrier, slow crystallization rate and low thermal stability, have

limited its wider applications [24]. Therefore, polymer blending and preparation of nanocomposites have often been employed to modify the physical properties of PLA in order to extend the practical applications [25 – 29]. Nanocomposites are a class of composites in which dimensions of the reinforcing phase are in the order of nanometers. The introduction of nanofillers, such as organo-modified layered silicates, silver, zinc oxide, graphite derivatives, carbon nanotubes, and silica, is a practical and feasible method to enhance the antibacterial, barrier, thermal, melt behaviour and mechanical properties of PLA [30 - 32].

1.2 Statement of the problem

The use of fossil fuels as a source of energy brings with it dangers such as environmental pollution and the challenge of such fuels being depleted, hence the need for alternative renewable energy sources. Conventionally, phosphors are immobilized in glues such as silicon and epoxy resin when applied in the LED emitter layer. This method experiences the challenges of difficulty in controlling the thickness of the emitter layer and the reproducibility of the emitted light.

Rare-earth (RE) doped phosphors immobilized into a polymeric matrix offers appealing alternatives for electro-optical systems, due to high photoluminescence combined with good physic-mechanical properties of the polymer. The group II – VI compound semiconductors (like SiO_2) have thus received special interest due to their novel physical properties and associated applications in optoelectronic devices.The synergy between the phosphor and polymer characteristics make for new composites, which could be applied in devices such as LEDs and full colour displays. Thus, the dispersal and immobilisation of SiO_2 based phosphors in the PLA polymer matrix.

1.3 General and specific objectives

The general objective of this study was to study the morphological, optical and luminescence properties of the SiO_2, SiO_2 singly doped (with Sr^{2+}) and SiO_2:Sr^{2+} co-doped (with Tb^{3+}) phosphors immobilized into the PLA matrix. In order to achieve this aim we formulated the following specific objectives:

- Preparation and characterization of SiO_2 nanoparticles doped with Sr^{2+} in order to study morphology, structure, defect centers and luminescence properties,
- Preparation and characterization of SiO_2 nanoparticles co-doped with Sr^{2+} and Tb^{3+} in order to study morphology, structure, luminescence properties and energy transfer mechanism between Sr^{2+} and Tb^{3+}, and
- Preparation and characterization of PLA:SiO_2 co-doped with Sr^{2+} and Tb^{3+} nanocomposites in order to study the structure, morphological, thermal and luminescence properties.

1.4 Outline of the dissertation

This dissertation comprises of six chapters:

Chapter 1: Background and objectives.

Chapter 2: Literature review.

Chapter 3: Colour tuning and white light emission from sol-gel SiO_2 nanoparticles doped with Sr^{2+}.

Chapter 4: Morphology, structural and luminescent properties of sol-gel synthesized SiO_2 powders co-doped with Sr^{2+} and Tb^{3+}.

Chapter 5: Characterization of PLA:SiO_2 co-doped with Sr^{2+} and Tb^{3+} nanocomposites.

Chapter 6: Conclusion and future work.

References

1. B. Moine, G. Bizarri, *Mater. Sci. and Eng.* B105 (2003) 2–7.

2. Z. Chen, J.H. Zhang, S. Chen, M.Y. Lin, C.Q. He, G.D. Xu, M.M. Wang, X.F. Yu, J.Q. Zou, *J. Alloys and Comps.* 632 (2015) 756 – 759.

3. Y. Yu, *Opt. Exp.* 19(20) (2011) 19473 – 19479.

4. H.A.A. Seed Ahmed, A. Yousif, H.C. Swart, R.E. Kroon, *Materials Today: Proceedings* 2 (2015) 4111 – 4117.

5. Jiann-Wen Huang, Yung Chang Hung, Ya-Lan Wen, Chiun-Chia Kang, Mou-Yung Yeh, *J. Appl. Polym. Sci.* 112 (2009) 1688–1694.

6. M. Kakihana, *Sol.-Gel Sci. Technol.* 6 (1996) 7 – 55.

7. N.Y. Turova, E.P. Turevskaya, Kessler, V. G.; M.I. Yanovskaya, *The Chemistry of Metal Alkoxides*; Kluwer Academic: Boston, 2002.

8. Q. Guodong, W. Minquan, W. Mang, F. Xianping, H. Zhanglian, *J. Lumin.* 75 (1997) 63 - 69.

9. D.M. Boye, C.P. Ortiz, A.J. Silversmith, N.T.T. Nguyen, K.R. Hoffmann, *J. Lumin.* 128 (2008) 888 - 890.

10. H.A.A. SeedAhmed, O.M. Ntwaeaborwa, R.E .Kroon, *J. Lumin*. 135 (2013) 15–19.

11. T. Jan, Z. Johannes, C. Rolf, *J. Mater. Sci*. 41 (2006) 8173.

12. A.J. Silversmith, D.M. Boye, K.S. Brewer, C.E. Gillespie, Y. Lu, D.L. Campbell, *J. Lumin.* 121 (2006) 14 – 20.

13. D. Jiang, J. Wen, M. Jia, Q. Guo, Z. Xiao, W. Luo, F. Pang, Z. Chen, T.

Wang, *Opt. Mater. Exp.* 8(6) (2018) 1593 - 1602.

14. K.G. Tshabalala, S.H. Cho, J.K. Park, S.S. Pitale, I.M. Nagpure, R.E. Kroon, H.C. Swart, O.M. Ntwaeaborwa, *J. Alloys Compd*. 509 (2011) 10115 - 10120.

15. L. Xiou, Y. Xie, M. He, Y. Chen, W. Li, W. Yu, *J. Rare Earths* 28 (2010) 225 - 228.

16. F. Zhenxiao, B. Wenbo, *Solid State Sci.* 10 (2008) 1062 - 1067.

17. O.M. Ntwaeaborwa, H.C. Swart, R.E. Kroon, P.H. Holloway, J.R. Botha, *J. Phys. Chem. Solids* 67 (2006) 1749 - 1753.

18. G.E. Malashkevich, G.I. Semkova, A.P. Stupak, A.V. Sukhodolov, *Phys. Solid State* 46 (2004) 1425 - 1431.

19. U. Caldin˜o, A. Speghini, E. A´ lvarez, S. Berneschi, M. Bettinelli, M. Brenci, G.C. Righini, *Opt. Mat.* 33 (2011) 1892 - 1897.

20. U. Caldin˜o, A. Speghini, M Bettinelli, *J. Phys. Condens. Matter*. 18 (2006) 3499.

21. E. Nakazawa, S. Shionoya, *J. Chem. Phys.* 47 (1967) 3211 - 3219.

22. S.S. Bari, A. Chatterjee, S. Mishra, *DOI 10.1080/15583724.2015.1118123*

23. J.W. Huang, Y. C. Hung, Y.L. Wen, C.C. Kang, M.Y. Yeh, *J. App. Polym. Sci.* 112, (2009) 1688–1694

24. D. Notta-Cuvier, J. Odent, R. Delille, M. Murariu, F. Lauro, J.M. Raquez, B. Bennani, P. Dubois, *Polym. Test.* 36 (2014) 1–9.

25. B.W. Chieng, N.A. Ibrahim, W.M.Z.W. Yunus, M.Z. Hussein, *Polymers* 6 (2014) 93–104.

26. V.S.G. Silverajah, N.A. Ibrahim, W.M.Z.W. Yunus, H.A. Hassan, B.W. Chieng, *Int. J. Mol. Sci.* 13 (2012) 5878–5898.

27. B.W. Chieng, N.A. Ibrahim, W.M.Z.W. Yunus, M.Z. Hussein, *J. Appl. Polym. Sci.* 130 (2013) 4576–4580.

28. B.W. Chieng, N.A. Ibrahim, W.M.Z.W. Yunus, M.Z. Hussein, V.S.G. Silverajah, *Int. J. Mol. Sci.* 13 (2012) 10920–10934.

29. B.W. Chieng, N.A. Ibrahim, W.M.Z.W. Yunus, *Polym. Plast. Technol. Eng. 51* (2012) 791–799.

30. M. Murariu, Y. Paint, O. Murariu, J.M. Raquez, L. Bonnaud, P. Dubois, *J. Appl. Polym. Sci.* 132 (2015) 42480.

31. C. Vasile, *Mater*. 11 (2018) 1834.

32. R.T. De Silva, P. Pasbakhsh, S.M. Lee, A.Y. Kit, *Appl. Clay Sci*. 111 (2015) 10–20.

Chapter 2 – Literature Review

2.1 Luminescence and Phosphors

Over the past decade, phosphor-converted white light-emitting diodes (pc-WLEDs) have been a topic of interest to scientists and engineers due to their outstanding luminous efficiency and brightness, low power consumption, reliability, long operation lives, and environmentally friendly characteristics. Compared to traditional lighting sources, such as incandescent, halogen, xenon, and fluorescent lamps, pc-WLEDs are regarded as the most encouraging and emerging next generation solid-state lighting (SSL) technology [1].

Luminescence is defined as a spontaneous emission of radiation or generation of light by a substance that is excited by an external source. The energy lifts the atoms of the material into an excited state, and then, because excited states are unstable, the material undergoes another transition, back to its unexcited ground state, and the absorbed energy is liberated in the form of either light or heat or both [2]. The excitation involves only the outermost electrons orbiting around the nuclei of the atoms. Luminescence occurs in visible region between the wavelengths of 300-650 nm.

There are two principal varieties of luminescence, fluorescence and phosphorescence, distinguished by the delay in reaction to external electromagnetic radiation as shown in Fig. 2.1. Fluorescence emission is seen to be taking place simultaneously with absorption of radiation and stopping immediately as radiation ceases. Phosphorescence involves a delayed emission of radiation following absorption [3]. The delay may take as much as several minutes, but phosphorescence continues to appear after the energy source has been removed.

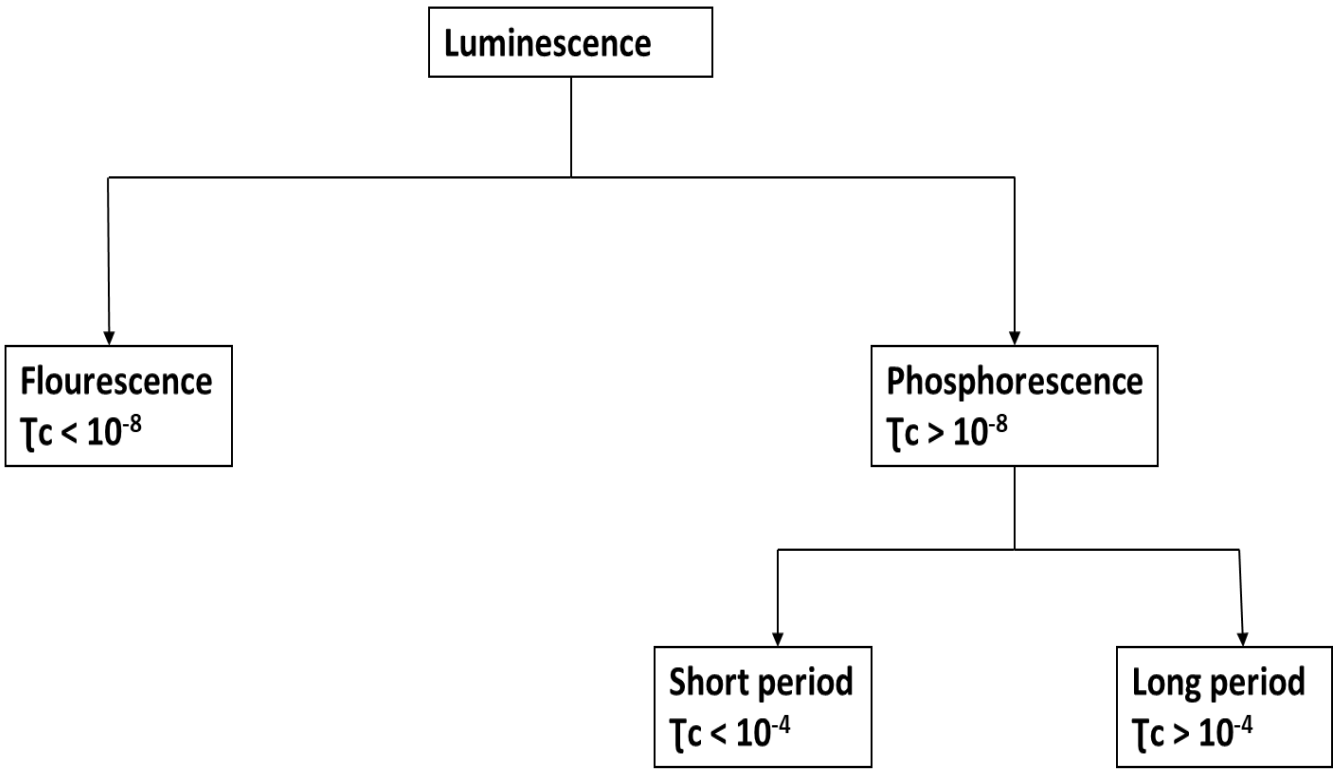

Fig. 2.1: Classification of luminescence based on duration of emission.

Luminescence has different types depending on the source of excitation, like:

- **Photoluminescence (PL)** where the emission of the light is the result of the excitation by electromagnetic radiation/photons. It is a less specific term, which embraces both fluorescence and phosphorescence. Photoluminescence has a very broad application area from whitening substances in washing powder to plasma screens for large-scale displays.
- **Thermoluminescence (TL)** that is also known as thermally stimulated luminescence (TSL). It is the luminescence activated thermally after initial irradiation by other means such as α, β, γ, UV or X-rays. It is not to be confused with thermal radiation: the thermal excitation only triggers the release of energy, imparted to the material from another source of excitation.

- **Radioluminescence (RL)** is the phenomenon by which light is produced in a material by bombardment with ionizing radiation such as beta particles, X-rays or gamma rays.
- **Sonoluminescence (SL)** that is the phenomenon by which light is produced due to the excitation by ultrasonic waves [3].

The focus of this research will be photoluminescence, which can be either intrinsic or extrinsic. Intrinsic luminescence refers to a situation in which the luminescence comes from within a pure material or crystal, while extrinsic luminescence refers to luminescence caused by intentionally incorporating impurities or defects into a phosphor [3].

Phosphors or luminescent materials are materials that exhibit the phenomenon of luminescence, i.e. they emit light when exposed to radiation such as ultraviolet light or an electron beam. Phosphors have several advantages over conventional incandescent and fluorescent lamps in power efficiency, long lifetime, non-pollution and design flexibility [4]. For potential use, phosphors should have strong absorption and excitation in the region from ultraviolet to blue and should emit the desired light.

Inorganic phosphors usually consist of a host material that could be an oxide, nitride, oxynitride, silicate, sulphide, selenide, halide or oxyhalide, doped with small amounts of activator ions like rare earth and/or transition metal ions [6]. The activator ions act as emission or luminescence centres and possess energy levels that can be populated by direct excitation or indirectly by energy transfer [6]. A good phosphor should absorb the excitation energy and emit light afterwards as fast and efficiently as possible, with the elapsed time between excitation and emission being short to avoid afterglow. Energy absorption can occur either at the activator ion or at a random place in the lattice, but eventually the energy should be transferred to the luminescent centre for the emission to occur. In this study silica (SiO_2) is used as the host matrix while terbium ion (Tb^{3+}) is the luminescent centre/activator.

2.1.1 Crystal field

The luminescent behavior of the RE^{3+} ions is generally influenced by their concentration and the chemical environment surrounding them [7]. The ligands around the RE ion creates a crystal filed on the ion, the strength of this crystal field is calculated with the following formula:

$Dq = ze^2r^4/6R^5$

Dq is the crystal field strength, *R* the distance between the ion and its ligands, *z* is the charge/valence of the anion, *e* the charge of an electron and *r* is the radius of the *d* wave function [8]. Based on the crystal field theory the *f* orbital electrons are not sensitive to the lattice environment due to shielding function of the electrons in the outer shell. However, the *d* orbitals are very sensitive to the crystal environment will split into two sets due to crytal degeneracy. The set with higher energy is designated as t_{2g}, while that with lower energy is e_g. The change in the crytal field strength manifests in the alteration of the splitting of the d orbitals thus impacting the shift (red or blue) in the PL emission peak [9].

2.2 Silica (SiO_2) as a host matrix

Silica (SiO_2) has proved to be a good host matrix for the RE elements because of its transparency, chemical and thermal stability dopant solubility and ease of production [10, 11]. SiO_2 is one of the most abundant materials on earth, present in the form of sand on all beaches and deserts. It may occur in crystalline (like α-quartz, β-quartz, α-cristobalite, β-cristobalite, α-tridymite, β-tridymite, γ-tridymite, coesite, melanophlogopite) or amorphous phase (like opal, hyalite, sintered pearl, lechateierite, natural silica glass). Naturally occurring SiO_2 is contaminated with minerals that makes it impossible to use it for technological applications. The basic structural unit of vitreous SiO_2 and silicate glasses is the SiO_4 tetrahedron. There are four oxygen atoms, one located at each apex of a regular tetrahedron and a single silicon atom is located at the centre of the tetrahedron [12]. The presence of defects in the silica matrix can

dramatically change its structural, electrical, and optical properties. Many parameters, such as manufacturing processes, irradiation, mechanical stress, change of temperature, and the presence of impurities may cause the formation of defects and/or lead to the transformation of the existing defects to other types of defect [12]. Defects in a perfect silica glass could include oxygen or silicon vacancies and their interstitials, Si−Si or O−O homobonds or under-coordinated silicon or oxygen atoms. The emissions from 378 to 540 nm are related to the intrinsic defects emission within the SiO_2 host [13, 14, 15 -17]. While the emission band at around 584 nm may be due to the oxygen interstitials (O_i) of the SiO_2 nanoparticles [14] or to carbon impurities that may come from the organic precursors [18, 19, 20].

The preparation method, the particle size and the morphology of phosphors frequently affect the optical properties of luminous materials [21]. The sol-gel technique produces microporous silica with high purity and that allows incorporation of much higher concentration of dopants than the melt process, thus rendering a more attractive host matrix silica [6]. The silicates prepared by solid-state reaction technique on the other hand are found to have large size distribution and irregular shape [22]. As one of the most well-known soft solution processes, so far the sol-gel technique has found a very extensive application for the design and synthesis of various kinds of advanced functional and engineering materials, including powders, films, fibres, and monoliths of almost any shape, size, and chemical composition, and of course, nanostructures and organicinorganic hybrids [11]. The sol-gel process involves the synthesis of an inorganic and/ or organic network by a chemical reaction in solution at low (generally ambient) temperatures followed by the transition from solution to colloidal sol and to a multiphasic gel form. According to the different precursors utilized, the sol-gel techniques can be divided into three types:

(1) The sol-gel route based upon hydrolysis-condensation of metal-alkoxides.

(2) The gelation route based upon concentration of aqueous solutions involving metal-chelates, often called as “chelate gel” route.

(3) The polymerizable-complex (PC) route [11].

Apart from the tetraethyl orthosilicate (silicon alkoxide), most of the metal alkoxides suffer from high cost, unavailability, toxicity, and fast hydrolysis rate (thus difficult in controlling the homogeneity of different components during experimental processes) [23].

2.3 Doping

Materials with a relatively wide band gap can be made to emit luminescence in the visible range by addition of different atoms or imperfections into the crystal [3]. This deliberate addition of ‘impurities’ is called doping and the ‘impurities’ are called dopants. Dopants are classified into various categories based on their function in host lattices due to their electronic configuration, solubility and structure of the host lattice:

- The **activator or luminescent centre** emits energy in the form of radiation when the electron from the dopant ion returns to ground state after excitation by absorption of energy.
- The **sensitizer** (in case of two dopants) absorbs most of the energy and transfers it to the activator for emission to occur.
- The **co-activator** is the dopant that does not luminesce but help in the process of luminescence by acting as charge compensator or by creating hole/electron traps [3].

Doping of SiO_2 with a very low percentage of lanthanide luminescent material in their nano-size cavities exhibits strong, intense, and stable fluorescence properties [24]. Moreover, dispersion of lanthanide-based nano-phosphor into silica matrix reduces the hazards of these inorganic nano-systems [25]. The RE^{3+} based luminescent materials have the following characteristics: their emissions are due to the unique 4f – 4f or 4f – 5d transitions of the RE^{3+},

the emissions have high colour purity due to shielding of 4f electrons by outer 5s and 5p electrons [26]. In addition, the host lattice has little influence on the positions of the 4f configuration energy levels [26].

2.3.1 Terbium

Terbium ion (Tb^{3+}) is among the lanthanide ions that have been recognised as the most efficient down-converting materials that convert UV light to visible emission [13]**.** Trivalent Tb^{3+} is a RE^{3+} ion it exhibit narrow line emissions located at 488, 543, 586 and 622 nm due $^5D_4 - {}^7F_J$ (J = 6, 5, 4, 3) transition, as shown in Fig. 2.2 [14]. These emissions result in relatively low intensities since they are parity and spin forbidden, and thus ways of increasing the emission intensities have to be explored. One way of increasing the intensities of the RE materials is by energy transfer. Energy transfer occurs more often when there is an overlap between the emission spectrum of the sensitizer (energy donor) and the absorption spectrum of the activator (energy acceptor) [14]. This transfer favours an interaction between a broadband donor and a broadband acceptor due to the anticipated optimal spectral overlap [14].

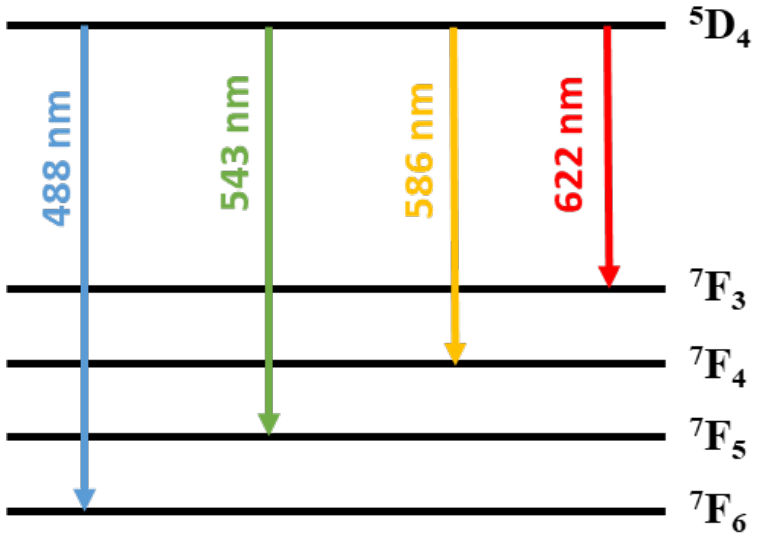

Fig. 2.2: Line emissions of Tb^{3+} ion.

Another challenge with the Tb^{3+} ions is that they exhibit strong absorption in the range 240-260 nm, which is difficult to access because of the short wavelength [27]. Thus, it can be advantageous to use sensitizers with their allowed transition occurring a longer wavelength. Several researchers used cerium ions as sensitizers because their allowed transition occurs at 320 nm, which corresponds to a more accessible and convenient wavelength region [10, 11, 15, 16, 17].

There has been studies on co-doping of RE^{3+} elements such as Tb^{3+}, Ce^{3+}, Eu^{3+}, Sm^{3+} etc. and energy transfer between these dopants in different host matrices. For example, Motloung *et al.* [28] reported the colour tuning and energy transfer pathways in $MgAl_2O_4$ triply doped with 0.1% Ce^{3+}, 0.1% Eu^{2+}, x% Tb^{3+} ($0 \leq x \leq 2\%$) nanocrystals synthesized using sol-gel process. They have observed that the PL results revealed the existence of the energy transfer from $Eu^{2+} \rightarrow Tb^{3+} \rightarrow Ce^{3+}$. Ntwaeaborwa *et al*. [10] reported on the enhanced luminescence and degradation of SiO_2:Ce^{3+}, Tb^{3+} powder phosphors prepared by a sol-gel process. They have realized enhanced green PL from Tb^{3+} ions due to co-doping with Ce^{3+} ions from SiO_2:Ce, Tb powder phosphors prepared by a sol-gel technique. Blue emission from the Ce^{3+} ions was completely suppressed by Tb co-doping, presumably due to energy transfer from $Ce^{3+} \rightarrow Tb^{3+}$ [10]. Ahmed *et al*. [11] reported on high efficiency energy transfer in Ce^{3+}, Tb^{3+} co-doped silica prepared by sol-gel method. There is however in our knowledge no reported studies on the co-doping of Tb^{3+} and Sr^{2+}.

2.3.2 Strontium

Strontium (Sr) is an alkaline earth metal with the [Kr] $5s^2$ electron configuration, thus it does not have electrons in the 4d orbital and cannot undergo excitation like the rare-earth/lanthanide

elements. The introduction of Sr^{2+} (which has a larger ionic radius than Si^{4+}) into the SiO_2 matrix affects the optical properties of SiO_2 by creating significant lattice defects as well as vacancies. In previous studies, Sr^{2+} was doped into different oxides like TiO_2, SnO_2 and ZnO [29, 30, 31]. The doping of TiO_2 with Sr^{2+} resulted in the increase in band gap and oxygen vacancies with increase in Sr^{2+} concentration [29]. The incorporation of Sr^{2+} into SnO_2 promoted the formation of singly charged oxygen vacancies because of the difference in the valence states of Sr^{2+} and Sn^{4+} [30]. While in the study of Sr^{2+} doped ZnO the optical band gap of ZnO decreased slightly with an increase in Sr^{2+} concentration that was due to the change of ZnO lattice distortion [31].

2.4 Composites

Composite are composed of constituent materials that have two main categories namely, the matrix (binder) and the filler. At least one representative from each category is needed to create a composite. The matrix phase embeds, surrounds, and supports the filler by preserving their relative locations. The fillers contribute their specific physical and mechanical assets, thus enhancing the properties of the matrix [32].

The composites can be classified at two different levels:

• The first criterion of classification is based on the matrix (binder) constituent. The main composite families encompass organic matrix composites (OMCs), metal matrix composites (MMCs), and ceramic matrix composites (CMCs). The term OMC generally refers to two classes of composites, namely, polymer matrix composites (PMCs) and carbon matrix composites, which are usually called carbon-carbon composites.

• The second classification criterion refers to the filler phases; here, fibre-reinforced composites (FRCs), laminar composites, or particulate composites are distinguished. FRC can be further

separated into those containing discontinuous or continuous fibres, respectively, as reinforcements [32].

Compared with well-established materials like metals, polymer matrix composites display the following characteristics high specific strength and high specific modulus, expedient fatigue resistance and high damage resistance, good damping characteristics and useful processing techniques [32, 33].

The immobilization of phosphor particles in different kinds of glues (such as silicon, polyurethane or epoxy resin) for LEDs experiences a challenge of controlling the emitter layer thickness and thus the reproducibility of the emitted light. Immobilizing the phosphor particles in a polymer matrix can overcome this challenge [34]. The incorporation of nanophosphor materials containing RE^{3+} ions into polymer matrix has attracted attention of researchers because this approach provides composite materials with improved PL properties, good thermal stability, excellent optical properties, impact resistance, low temperature processibility, flexibility and ability to form thin films [35 -37].

Several methods have been used to prepare luminescent polymer composites such as in situ polymerization, solution casting, and melt processing [38 - 40]. During in situ polymerization, the nanoparticles are premixed with the liquid monomer or monomer solution. Then, either heat, radiation or suitable initiators initiate polymerization [40]. The solution casting method is based on a solvent system in which the polymer or pre-polymer is soluble. The polymer is usually dissolved in a suitable solvent while the nano-particles are dispersed in the same or a different solvent before the two are mixed, the subsequent evaporation of the solvent results in the formation of the nanocomposite [40]. In the melt processing technique, the nanoparticles are mixed with the polymer in the molten state. This method is environmentally benign due to the absence of organic solvents and it is compatible with current industrial processes, such as

extrusion and injection molding [37, 40]. Two primary factors determine the level of dispersion of the nanoparticles within the polymer matrix during melt processing: (i) enthalpic interaction between the polymer and the nanoparticle and (ii) processing conditions [40].

Several studies have been done on polymer phosphor composites [34 - 36]. In the research on the composite based on $Ba_2SiO_4:Eu^{3+}$-doped Polyvinylidene fluoride (PVDF) polymeric membrane the research concluded that the composite could be successfully applied in optical devices as light-emitting diodes [34]. While in the study of Polystyrene (PS) films embedded with $ZnO:Tb^{3+}$ nanophosphor it was observed that the PL properties increased with increasing nanophosphor concentration. Furthermore, the temperature-dependent PL study of the nanocomposite films showed that the PL intensity decreased with increasing temperature due to thermal quenching [35]. The Poly methyl methacrylate (PMMA)/$Gd_2O_3:Eu^{3+}$ composites on the other hand were found to exhibit characteristic red phosphorescence from electronic transitions in trivalent europium ions. Quite good quantum efficiencies, from 23% to 35%, are achieved, suggesting promising applications for these composites [36].

The polymer matrix used in this study is Polylactic acid (PLA) which is a linear aliphatic thermoplastic polyester that has obtained much attention because it is biodegradable, environment friendly and from renewable resource. However, its brittleness and low crystallization rate are major defects for many applications [41]. Polymers from renewable resources have attracted increasing attention due to two major reasons: firstly environmental concerns, and secondly, the realization that petroleum resources are finite. PLA is prominent due to versatility of its applications and relatively low cost of production at industrial scale [39]. Most of the research is based on polymer blending and preparation of nanocomposites to modify the physical properties of PLA in order to extend the practical applications [39 - 44].

However, in our knowledge there are no studies that have looked at the luminescence of the PLA SiO_2 phosphor nanocomposites.

Reference

1. Q. Zhou, L. Dolgov, A. M. Srivastava, L. Zhou, Z. Wang, J. Shi, M. D. Dramićanin, M. G. Brik, M. Wu, *J. Mater. Chem. C* 6 (2018) 2652-2671.
2. S.E. Braslavsky, *Pure Appl. Chem.*, 79 (3) 2007 293–465.
3. K.V.R. Murthy, H.S. Virk, *Defect and Diffusion Forum* 347 (2014) 1-34.
4. L.S. Rohwer, A.M. Srivastava, *Electrochem. Soc. Interface* 12 (2003) 36 - 39.
5. H. He, R. Fu, X. Song, D. Wang, J. Chen, *J. Lumin*. 128 (2008) 489 – 493.
6. T. Justel, H. Nikol, C. Ronda, *Angew. Chem. Int. Ed.* 37 (1998) 3084 – 3103.
7. T. Kim, Y. Yoon, D. Kil, Y. Hwang, H. Chung, I.H. Kim, Y. Ahn, *Mater. Lett.* 47 (2001) 290
8. P.D. Rack, P.H. Holloway, *Mater. Sci. Eng.* 21(4) 1998 171 – 219.
9. Y.Penghui, Y. Xue, Y. Honghing, J. Tingming, Z. Dacheng, Q. Jianbei, *J. Rare Earths*, 30(12) 2012 1208 – 1212.
10. M. Ntwaeaborwa, H.C. Swart, R.E. Kroon, P.H. Holloway, J.R. Botha, *J. Phys. and Chem. of Solids* 67 (2006) 1749–1753
11. A.A. Seed Ahmed, O.M. Ntwaeaborwa, R.E. Kroon, *J. Lumin.* 135 (2013) 15–19.
12. R. Salh (2011). Silicon Nanocluster in Silicon Dioxide: Cathodoluminescence, Energy Dispersive X-Ray Analysis, Infrared Spectroscopy Studies, Crystalline Silicon - Properties and Uses, S. Basu (Ed.), ISBN: 978-953-307-587-7.
13. C.E. Allred, E.R. Menzel, *Forensic Sci. Int.* 85 (1997) 83–94.
14. M. Saifa, M. Shebla, A.I. Nabeel, R. Shokry, H. Hafez, A. Mbarek, K. Damak, R. Maalej, M.S.A. Abdel-Mottale, *Sensors and Actuators B* 220 (2015) 162–170.
15. M. Saif, *J. Lumin.* 135, (2013) 187-195.
16. M.S. Dhlamini, O.M. Ntwaeaborwa, H.C. Swart, J.M. Ngaruiya, K.T. Hillie, *Physica B: Condensed Matter* 404 (22), (2009) 4406-4410.

17. D. Jiang, J. Wen, M. Jia, Q. Guo, Z. Xiao, W. Luo, F. Pang, Z. Chen, T. Wang, *Opt. Mater. Exp.* 8(6) (2018) 1593 – 1602.Y. Han, J. Lin, H. Zhang, *Mater. Lett.* 54 (2002) 389–396.
18. J.R. Martinez, S. Palomares-Sanchez, G. Ortega-Zarzosa, F. Ruiz, Y. Chumakov, *Mater. Lett.* 60 (2006) 3526–3529.
19. A.E. Abbass, H.C. Swart, R.E. Kroon, *J. Lumin.* 160 (2015) 22–26.
20. K.Y. Jung, H.W. Lee, H. Jung, *Chem. Mater.* 18 (2006) 2249 – 2255.
21. C. Guo, Y. Xu, F. Lv, X. Ding, *J. All. Comps.* 497 (2010) L21 –L24.
22. J. Lin, M. Yu, C. Lin, X. Liu, *J. Phys. Chem. C* 2007, 111, 5835-5845.
23. J.A. Gonzalez-Ortega, E.M. Tejeda, N. Perea, G.A. Hirata, E.J. Bosze, J. McKittrick, *Opt. Mater.* 27 (2005) 1221–1227.
24. G. E. Malashkevich, G. I. Semkova, A. P. Stupak, A. V. Sukhodolov, *Phys. Solid State* 46(8) (2004) 1425–1431.
25. U. Caldiño, A. Speghini, E. Álvarez, S. Berneschi, M. Bettinelli, M. Brenci, G. C. Righini, *Opt. Mater*. 33 (12) (2011) 1892–1897.
26. B. V. Ratman, M. Jayasimhadri, G. B. Kumar, K. Jang, S. S. Kim, Y. I. Lee, J. M. Lim, D. S. Shin, T. K. Song, J. Alloys Compd. 564(1) (2013) 100–104.
27. S.V. Motloung, B.F. Dejene, O.M. Ntwaeaborwa, H.C. Swart, R.E. Kroon, *Chem. Phys.* 487 (2017) 75–86.
28. N. Rajamanickam, S.S. Kanamni, S. Rajashabala, K. Ramachandran, *Mater. Lett*. 161 (2015) 520–522.
29. N. Wang, W. Zhou, Y. Liang, W. Cui, P. Wu, J. Mater. Sci. Mater. Electron. 26 (2015) 7751–7756.
30. S. Lakshmana Perumal, P. Hemalatha, M. Alagara, K.N. Pandiyaraj, *IJCPS* 4 (2015) 1–13.
31. M. M. Dawoud, H. M. Saleh, In Characterizations of Some Composite Materials, ed. by H. El-Din, M. Saleh, M. Koller, 2019 London, UK, IntecOpen.

32. R.M. Christensen, 2005. Mechanics of Composite Materials. Mineola, New York.

33. A.G. Bispo-Jr, N.A. Oliveira,, C.X. Cardoso, S.A.M. Lima, A.E. Job, I.O. Osorio-Román, C.S. Danna, A.M. Pires, *Mater. Chem. Phys*. 217 (2018) 160–167.

34. J. Prakash, V. Kumar, L. J. B. Erasmus, M. M. Duvenhage, G. Sathiyan, S. Bellucci, S. Sun, H.C. Swart, *ACS Appl. Nano Mater*. 1 (2018) 977−988.

35. Ž. Antic, R. Krsmanovic, M. Marinovic-Cincovic, M.D. Dramicanin, *Acta Physica Polonica A* 117 (2010) 831 – 836.

36. S.B. Mishra, A.K. Mishra, N. Revaprasadu, K.T. Hillie, W.J. vd. M. Steyn, E. Coetsee, H.C. Swart, *J. Appl. Polym. Sci.* 112 (2009) 3347–3354.

37. M.L. Saladino, A. Zanotto, D. Chillura Martino, A. Spinella, G. Nasillo, E. Caponetti, *Langmuir* 26 (2010) 13442−13449.

38. A. Potdevin, G. Chadeyron, S. Thérias, R. Mahiou, *Langmuir* 2012, 28, 13526−13535

39. V. Ojijo, S. S. Ray, *Prog. Polym. Sci.* 38 (2013) 1543– 1589.

40. J. Huang, Y.C. Hung, Y. Wen, C. Kang, M. Yeh, *J. Appl. Polym. Sci.* 112 (2009) 1688–1694.

41. N.A. Ali, *IJABR* 7 (2) 2017: 391-395.

42. B.W Chieng, N.A. Ibrahim, W.M.Z.W Yunus, M.Z. Hussein, *Polymers* 6 (2014) 93–104.

43. V.S.G. Silverajah, N.A. Ibrahim, W.M.Z.W. Yunus, H.A. Hassan, B.W. Chieng, *Int. J. Mol. Sci.*13 *(*2012) 5878–5898.

44. B.W Chieng, N.A. Ibrahim, W.M.Z.W Yunus, M.Z. Hussein, *J. Appl. Polym. Sci.* **2013**, *130*, 4576–4580.

Chapter 3 - Colour tuning and white light emission from sol-gel SiO_2 nanoparticles doped with Sr^{2+}.

(Published in *Materials Chemistry and Physics* 242 (2020) 122409)

3.1. Introduction

Research on phosphors spans over a century, but there is still a need for new phosphors. Factors such as new technological advances, the necessity of increasing the efficiency of white light-emitting solid state devices, which are an alternative lighting source and a possible new generation of lighting lamps, and changes in excitation sources (e.g. from electronic or ultraviolet excitation to excitation in vacuum) bring about this need [1,2]. In recent years, solid state lighting has become an interesting field for researchers, especially with respect to white light emitting diodes (w-LEDs) as replacement for conventional incandescent and fluorescent lamps. This is because solid-state lighting possesses advantages like environment-friendliness, brightness, fast response, low power consumption, longevity, reliability and excellent low temperature performance [3–6]. Single phosphors directly yielding white light emission are better than obtaining it from a mixture of individual red, green and blue phosphors, as the latter is hampered by reabsorption of the blue light [7]. Given this disadvantage and inspired by the possibility of synthesizing white light phosphor by singly doping the host material with ions such as Sr^{2+}, this study was undertaken to dope SiO_2 with Sr^{2+}. Amorphous SiO_2 has been investigated as an alternative to crystalline hosts for X-ray scintillators because of its advantageous mechanical properties (e.g. fibre drawing), its chemical stability, non-hygroscopic nature, and the possibility of incorporating larger concentrations of luminescent ions [8]. Selecting a cation (Sr^{2+}) with larger ionic radius (1.21 Å [9]) and lower valence charge than Si^{4+} (0.26 Å [9]) as dopant will create significant lattice defects as well as vacancies, which could affect optical properties of SiO_2. There are previous studies where Sr^{2+} was doped

into TiO_2 [10], SnO_2 [11] and ZnO [12]. Rajamanikam et al. [10] doped Sr^{2+} into TiO_2 nanoparticles and observed an increase in band gap and oxygen vacancies with an increase in Sr^{2+} concentration. Similarly, Wang et al. [11] found that the incorporation of Sr^{2+} into SnO_2 could promote the formation of singly charged oxygen vacancies due to the difference in the valence states of Sr^{2+} and Sn^{4+}. In the Sr^{2+} doped ZnO carried out by Lakshmana Perumal et al. [12], the results showed that the optical band gap of ZnO nanoparticles decreased slightly with an increase in Sr^{2+} concentration. This was attributed to the change of ZnO lattice distortion, which can generate more defects in the ZnO lattice. As far as Sr^{2+} doping into SiO_2 is concerned, no reports (if not none) occur in the literature to date.

In this study, a simple sol–gel method was used to synthesize Sr^{2+} doped SiO_2 phosphors that could be used as an alternative material in W- LEDs. As an option to melted glass, the sol–gel process was found to be an efficient technique for the synthesis of phosphors due to the good mixing of starting materials and relatively low reaction temperature [13–16]. In this work, it was also found that Sr^{2+} induces more defects in SiO_2 lattice. It was very interesting to observe that the Sr^{2+} doped SiO_2 exhibits emission peaks at around 378, 412, 442, 490, 540 and 580 nm, which were related to the intrinsic defects emissions within the SiO_2 host material [14, 17, 18].

3.2. Experimental

The sol-gel synthesis was carried out as reported elsewhere [14, 19]. SiO_2 was prepared using 99% tetraorthosilicate ($Si(OC_2H_5)_4$, TEOS) (from Merck), 95% ethanol (C_2H_5OH, EtOH), 55% nitric acid (HNO_3) (from Sigma-Aldrich) all of which were analytic grade and distilled water. TEOS (10 mL) and EtOH (10 mL) were combined and stirred for about 10 min. Then HNO_3 (5 mL) and distilled water (14 mL) were added to the solution and the mixture was stirred at

room temperature until gel point. However, in synthesizing Sr^{2+} doped SiO_2, the combined solution (of TEOS, EtOH, HNO_3 and distilled water) was stirred for 1 h. Thereafter, various masses of strontium acetate (from Sigma-Aldrich and analytic grade), previously dissolved in 5 mL of ethanol were added and the mixture was further stirred until gel point. The volume ratio of TEOS: EtOH: H_2O: HNO_3 was kept constant at 1:1:1.4:0.5 for all samples before the addition of the strontium acetate. The gels were then dried at room temperature in the air for approximately 24 h. The air-dried gels were crushed to fine powder using a mortar and pestle and heat treated at 100 C for 2 h to remove solvent and organic ligands and in order to obtain full densification. The powders were re-crushed and annealed at 800 C for 2 h under nitrogen, then further crushed and packaged for characterization. SiO_2 powders were annealed in nitrogen to prevent OH to diffuse in SiO_2 surface. Nitrogen is fairly inert, so it can leave the surface intact.

The structural properties of the samples were observed with a Bruker AXS Discover diffractometer with Cu Kα (1.54 Å) radiation. The morphology of the prepared nanoparticles was determined with a Zeiss SUPRA 55-VP scanning electron microscope (SEM) and Shimadzu model ZU SSX-550 Superscan energy dispersive X-ray spectrometer (EDS) was used for elemental composition analysis. Transmission electron microscopy (TEM) observation was performed with JEOL JEM 2100 transmission electron microscope. The diffuse reflectance measurements were carried out in the 200–800 nm wavelength range using a PerkinElmer UV–vis Lambda 950 spectrophotometer. The photoluminescence (PL) measurements were done with a 325 nm He–Cd laser system.

3.3. Results and discussion

3.3.1. Structural and compositional analysis

The XRD patterns of the SiO_2: xSr^{2+} ($0 \leq x \leq 10$ mol%) samples are shown in Fig. 3.1. The diffraction band with 2θ value centered at around 22° can be associated with the amorphous SiO_2 structure (JCPDS 36- 1451) [20]. No diffraction peaks related to strontium acetate or strontium silicate (Sr_2SiO_4) can be observed at low molar concentrations of Sr^{2+}, $x \leq 0.2$ mol%. However, at higher Sr^{2+} concentrations ($x \geq 0.4$ mol%), the low intensity peaks are observed around $2\theta = 31^{o}$ which were assigned to orthorhombic Sr_2SiO_4 (JCPDS 76-1493) [21]. It is clear that the intensity of peaks associated with Sr_2SiO_4 increased with increasing amount of dopant and, at x = 10 mol%, the amorphous structure seems to be almost transformed into crystalline Sr_2SiO_4. Therefore, it is concluded that the increase in Sr^{2+} concentration results in the transformation of amorphous SiO_2 to crystalline Sr_2SiO_4.

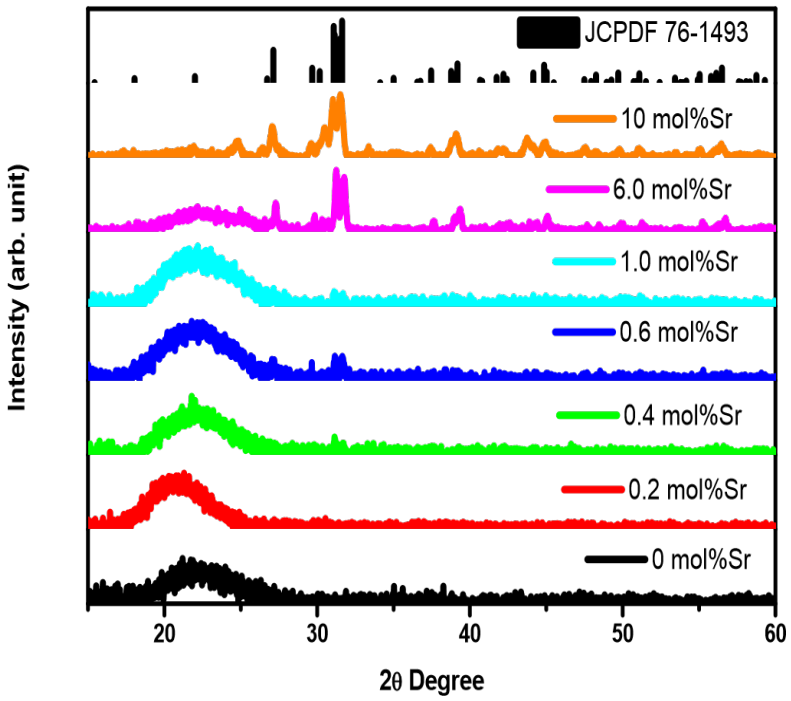

Fig. 3.1: X-ray powder diffraction patterns for the SiO_2: x Sr^{2+} ($0 \leq x \leq 10$ mol%) nanocrystals.

The SEM images of the selected SiO_2: x mol% Sr^{2+} (where x = 0, 0.4, 1.0 and 10) samples are shown in Fig. 3.2. All the images show irregular agglomerated particles, though the agglomeration appears to decrease with increasing Sr^{2+} concentration. The reduction in agglomeration may be related to the observed change in structure shown by the XRD results in Fig. 3.1. Generally, varying the Sr^{2+} concentration does not significantly influence the morphology of the prepared samples.

The chemical composition of the selected SiO_2:x mol% Sr^{2+} samples are shown in Fig. 3.3. The samples consist of only Si, O and Sr (with the Sr peak not present on the undoped (x = 0) sample (see Fig. 3.3(a)). The additional carbon (C) peak may be due to the carbon tape used to hold the samples during SEM/EDS measurement and/or the organic precursors. The fact that no traces of other elements were found in the spectra confirms the purity of the samples and correlates very well with XRD results shown in Fig. 3.1. The elemental maps showing the distribution of elements present in the selected SiO_2:x mol% Sr^{2+} samples were obtained, as given in Fig. 3.4. In Fig. 3.4 (a), the homogeneous distribution of both Si and O in the host sample is evident, while the Sr distribution appears not to be as homogeneous in Fig. 3.4 (b).

The TEM images of the selected x = 0, 0.4 and 10 mol% Sr^{2+}-doped nanoparticles are presented in Fig. 3.5. These micrographs clearly show that these samples consist of highly agglomerated particles, as it was observed in SEM results (see Fig. 3.2). In Fig. 3.5 (d), a higher magnification of the x = 10 mol% Sr^{2+} sample is presented, where well-defined lattice fringes are seen, revealing the crystalline nature of the sample. Thus, TEM results support the XRD data in Fig. 3.1. Both the TEM and XRD results confirm a transition from amorphous to crystalline structure as the Sr^{2+} mol% concentration increases.

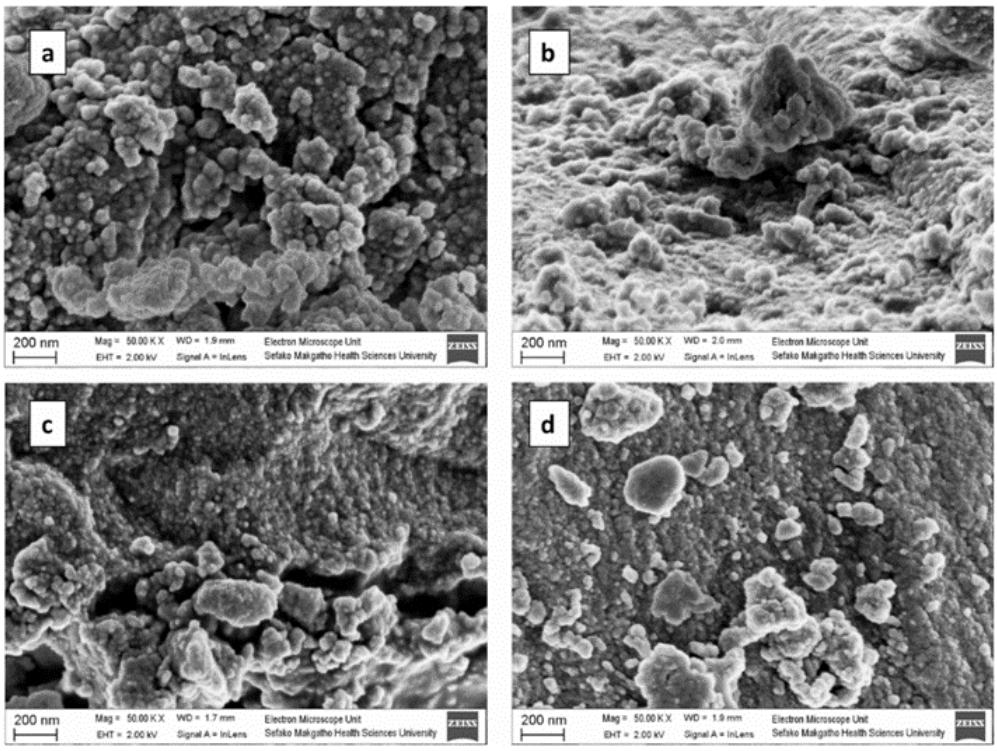

Fig. 3.2: SEM images of the SiO_2:x mol% Sr^{2p} (a) x ¼0 (host) (b) 0.4 (c) 1.0 and (d) 10 nanoparticles.

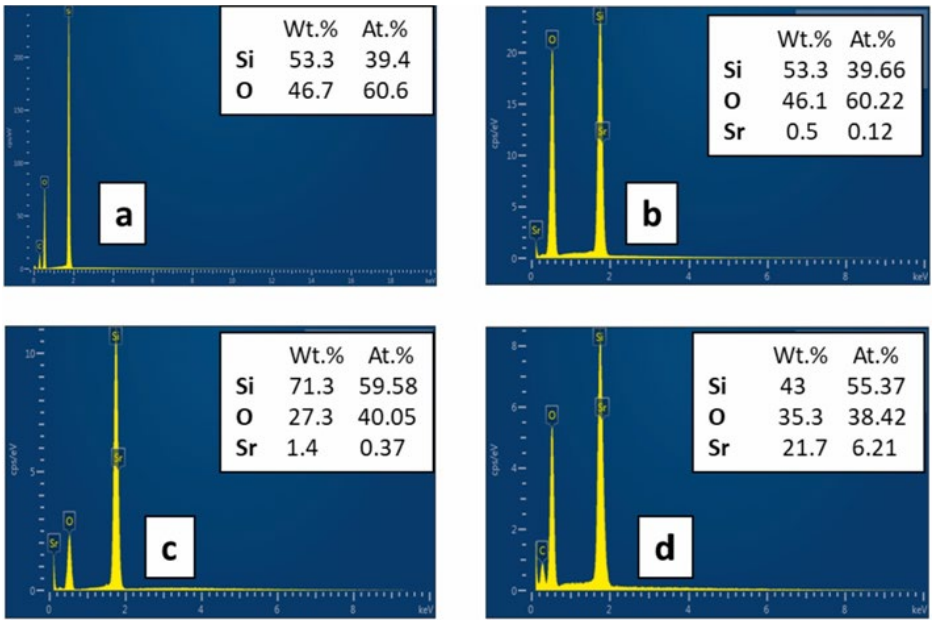

Fig. 3.3: EDS spectra of the SiO_2:x Sr^{2+} (a) x ¼0 (host) (b) 0.4, (c) 1.0 and (d) 10 mol% Sr^{2+}.

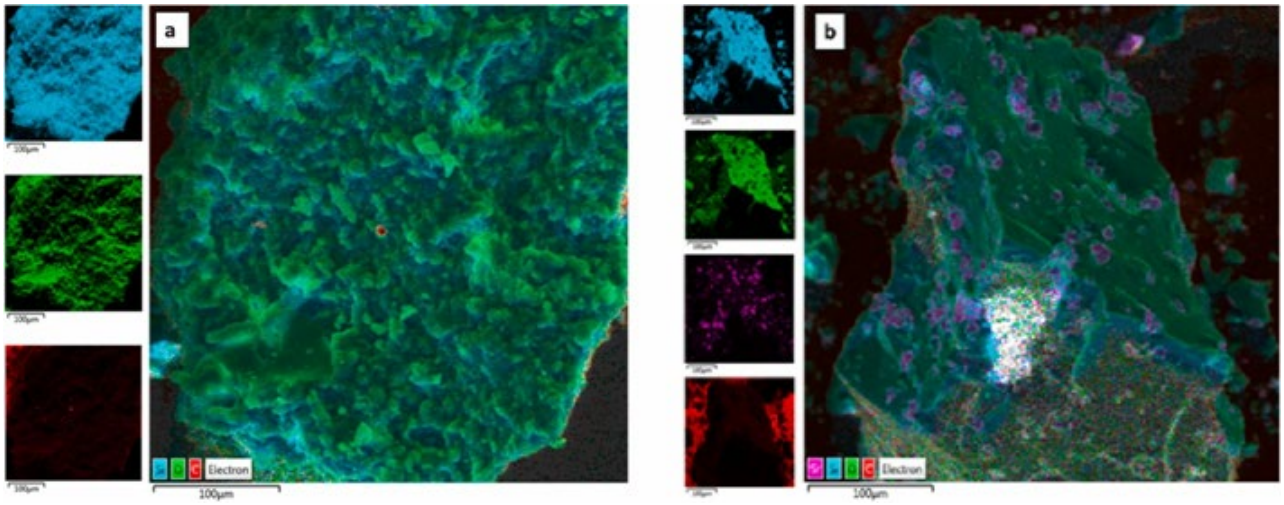

Fig. 3.4: Elemental map for the SiO_2:x Sr^{2+} (a) x = 0 (host), (b) 10 mol% Sr^{2+}.

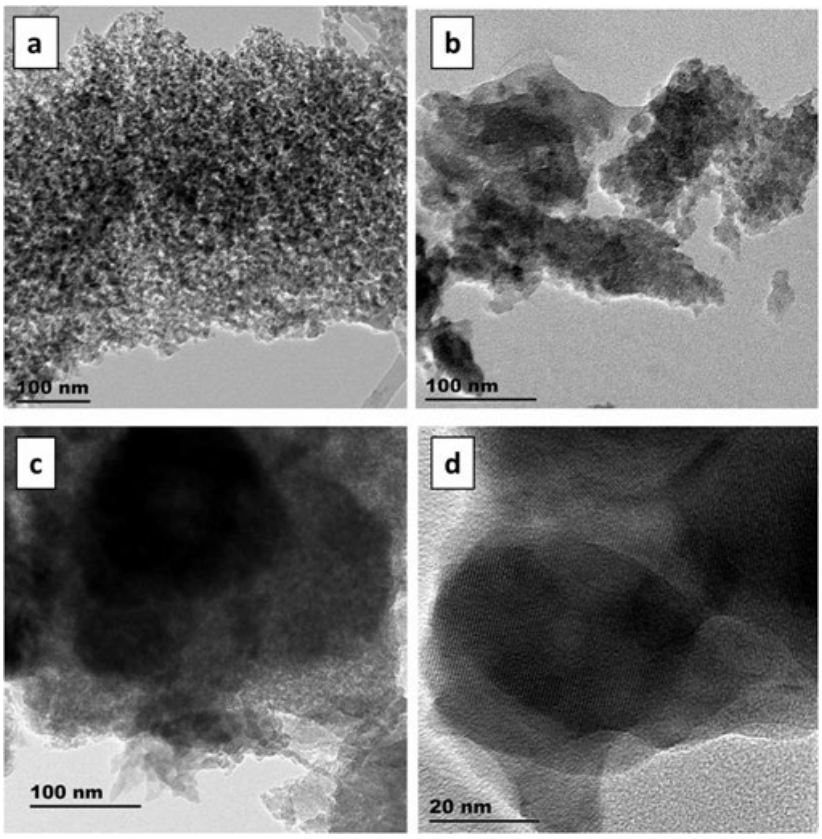

Fig. 3.5: TEM images of the SiO_2:x Sr^{2+} (a) x = 0 (host), (b) 0.4, (c) 10 mol% Sr^{2+} and (d) zoomed version of the x = 10 mol% Sr^{2+} doped samples.

3.3.2. Ultraviolet–visible (UV–vis) spectroscopy

The UV–vis diffuse reflectance spectra of the as prepared samples are presented in Fig. 3.6. The spectrum recorded for the undoped SiO_2 shows absorption peaks at around 238 and 253 nm that are due to B2-centre and non-bridging oxygen hole centre, respectively [22,23]. Furthermore, the undoped SiO_2 has another absorption edge at around 430 nm, which can be assigned to the oxygen vacancy related defects [22]. There is a red shift of the absorption edge at 430 nm with an increase in the Sr^{2+} dopant concentration.

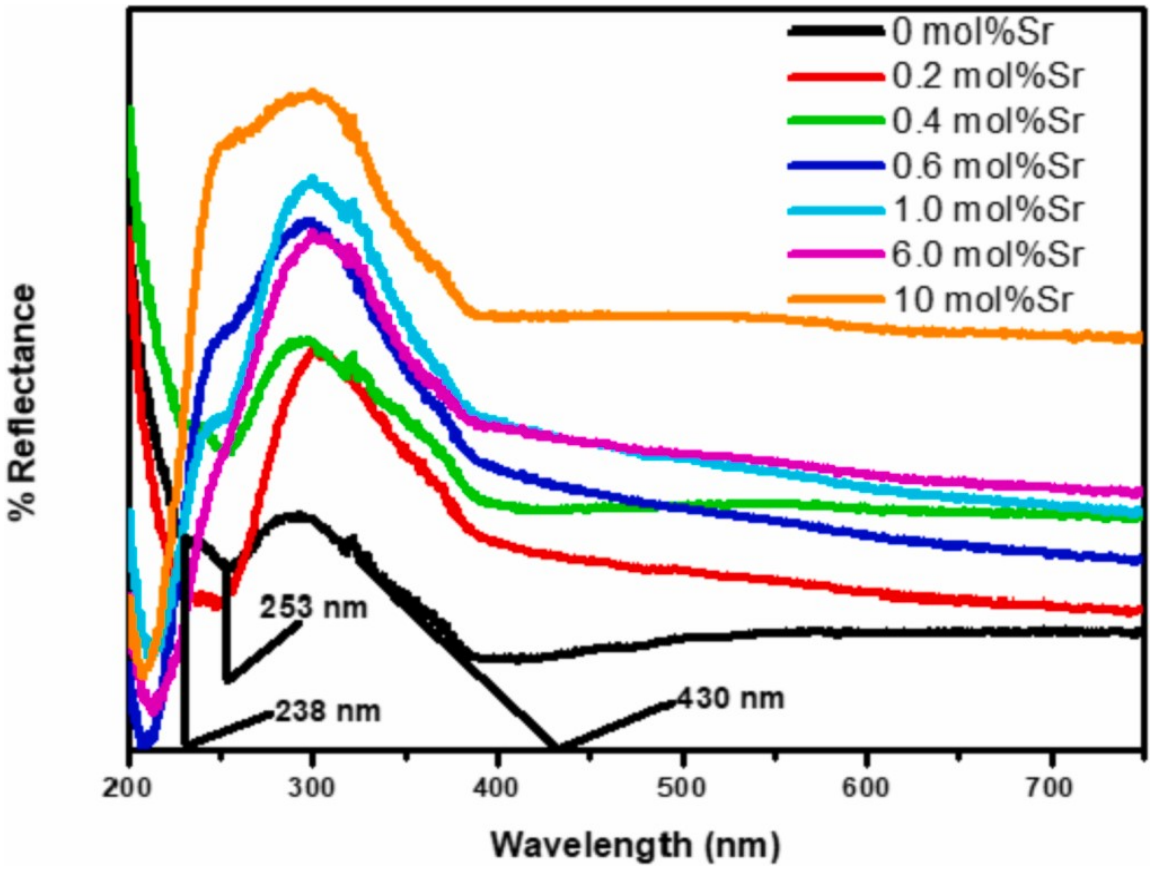

Fig. 3.6: Diffuse reflectance spectra of the SiO_2: x Sr^{2+} ($0 \leq x \leq 10$ mol% Sr^{2+}).

3.3.3. Photoluminescence (PL)

Fig. 3.7 (a) is the photoluminescence (PL) spectrum of the SiO_2 excited at 325 nm using a He–Cd laser at a room temperature. Two peaks were observed, a broad asymmetric emission band with a maximum at around 416 nm was observed and the second order peak at 650 nm. To understand better the properties of the PL emission band and its dependence on the structural order-disorder of the lattice, the multi-peak deconvolution of this band with the Gaussian fit function is shown in Fig. 3.7 (b). This result indicated that the broad band for the host emission is composed mainly of violet 3.25 eV (381 nm), blue 2.99 eV (415 nm) and 2.72 eV (456 nm), and green 2.51 eV (494 nm) and 2.21 eV (561 nm) bands. A number of researchers reported that undoped SiO_2 nanoparticles could emit in the violet, blue, green and infrared spectral regions [22, 24]. Rahman et al. [24] reported on the size dependent physicochemical and optical properties of silica nanoparticles. The PL spectra showed two main bands located in the green (~527 nm) and blue (~433 nm). Reisfeld et al. [18] reported peaks at 393, 409 and 450 nm, Koao et al. [17] reported peaks at 422, 448, 471 and 540 nm, while Han et al. [19] observed peaks at 382, 406 and 420 nm for pure SiO_2, which are comparable to the peaks observed in Fig. 3.7(b). Shaymardanov et al. [17] noted that amorphous SiO_2 nanoparticles show PL in the range 360–700 nm with maxima around 400 and 460 nm. The short wavelength band was attributed to organic substances adsorbed on the surface and the long wavelength band being due to SiO_2 defects. In this work, the observed peaks in Fig. 3.7(b) at around 376 nm in UV region is due to Si–O–C species (carbon-related species) defects [25]. The peaks in blue region 416 nm and 464 nm are neutral oxygen vacancies (blue) [22, 24]. Additionally, the peaks in green region 514 nm and 551 nm are assigned to the presence of hydrogen related species [24–26].

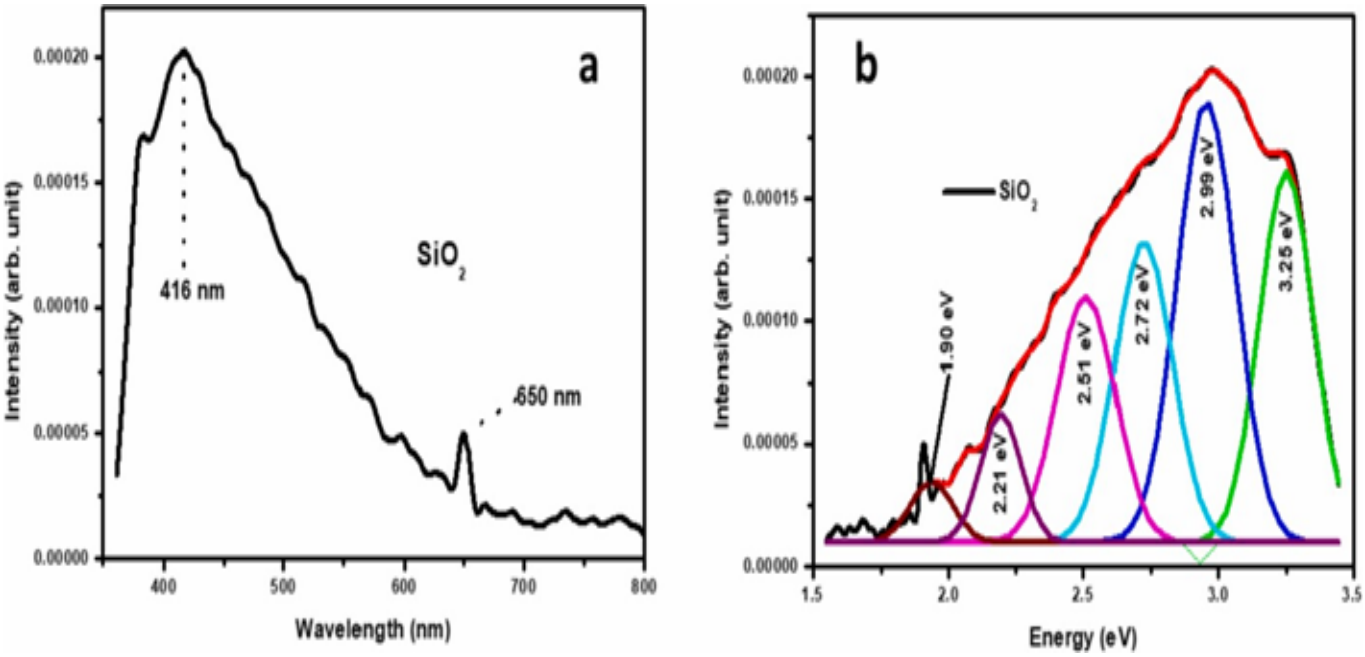

Fig. 3.7: The (a) emission and (b) deconvoluted spectrum of the SiO_2 host.

The PL emission spectra of the SiO_2:x Sr^{2+} ($0 \leq x \leq 10$ mol%) samples are shown in Fig. 3.8 (a). The incorporation of Sr^{2+} ions affected the luminescence intensity and emission position. In order to show the effects of varying the Sr^{2+} concentration on the emission wavelength, the normalized emission is presented in Fig. 3.8 (b). The nanoparticles with x = 0.2–0.6 mol% Sr^{2+} show asymmetric PL spectra with two peaks at around 490 and 540 nm. This shift in luminescence phenomenon from that of the x = 0 (host) may be attributed to the transformation of the existing defects in SiO_2 to other type of defects due of the presence of the Sr^{2+} dopant which has a bigger ionic radius as compared to Si^{4+}. However, as the dopant concentration increase from 1.0 to 10 mol% Sr^{2+}, a shift toward lower wavelength is observed (from green to the blue region).

The luminescence intensity as a function of Sr^{2+} concentration for the emission peak at 540 nm is represented Fig. 3.8 (c). The highest luminescence intensity was obtained at x = 0.4 mol% Sr^{2+} and, above this optimal dopant concentration, a reduction appears in luminescence intensity. It is clear that above this optimum dopant concentration there is a reduction in the

luminescence intensity. This intensity reduction can be attributed to well-known concentration quenching [27], which is one of the possible interactions that reduce luminescence in material, over and above, energy transfer to matrix, as well as non-radiative vibrational excitation of residual hydroxyl group [28,29].

In Fig. 3.8 (d), the deconvoluted PL spectrum of the SiO_2 doped with x = 0.4 mol% Sr^{2+} using Gaussian peak fit is shown. The emission spectra of SiO_2:xSr^{2+} phosphors at 0.2–0.6 mol% are composed of asymmetric broadband spectra that are generated by a number of emission bands. The emissions from 378 to 540 nm are related to the intrinsic defects emission within the SiO_2 host, as discussed above [19, 20, 22–24]. The emission band at around 584 nm may be due to the oxygen interstitials (O_i) of the SiO_2 nanoparticles [20]. Other researchers have attributed this broad band centred at about 584 nm to carbon impurities that may come from the organic precursors [30]. This emission at around 584 nm still needs for further study. In this work, it is very interesting to observe that the incorporation of Sr^{2+} into SiO_2 could promote the formation of more defects in the SiO_2 lattice due to difference in the valence states of Sr^{2+} and Si^{4+}.

The CIE results are given in Fig. 3.9 for the 0 x 10 mol% Sr^{2+} excited at 325 nm and the corresponding chromaticity coordinates (x; y) for the visible range are listed in Table 3.1. The colour shifts from blue to white at lower Sr^{2+} molar concentrations (i.e. x = 0.2–0.4 mol% Sr^{2+}), and then shifted back to the blue region as the Sr^{2+} molar concentration increases at x > 0.4 mol%. To determine the shades of white light produced by SiO_2:xSr^{2+} (x = 0.2 and 0.4 mol%) nanophosphors, the correlated colour temperature (CCT) values were calculated using McCamy equation:

$$CCT = 449n^3 + 3525n^2 - 6823.3n + 5520.33$$

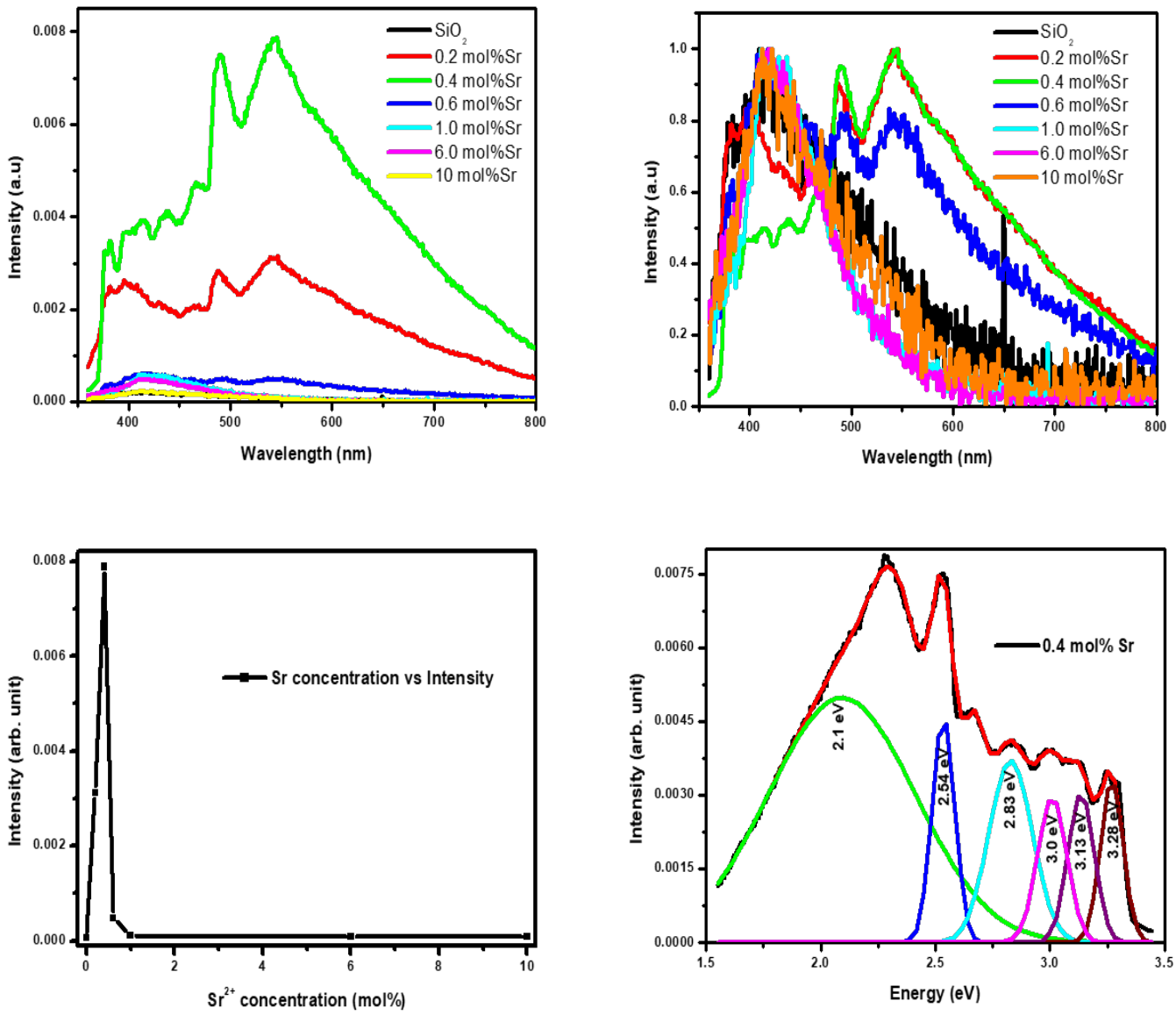

Fig. 3.8: (a) Emission spectra of the SiO_2:x Sr^{2+} ($0 \leq x \leq 10$ mol%) series, (b) normalized emission spectra of the series, (c) intensity as a function of Sr^{2+} concentration at 540 nm and (d) deconvoluted emission spectrum of x = 0.4 mol% Sr^{2+}.

where $n = (x - x_e)/(y - y_e)$ is the inverse slope of the line, which is defined from the chromaticity epicentre given as $x_e = 0.3320$ and $y_e = 0.1858$ while x and y are the chromaticity coordinates of the synthesized phosphor [31]. The correlated colour temperature (CCT) values of SiO2:$x$$Sr^{2+}$nanophosphors under excitation wavelength of 325 nm were found to be 5892 K and 5493 K respectively. The obtained CCT values are in the cool-white region. The CIE

results are consistent with the PL emission spectra as shown in Figs. 3.7 and 3.8. Generally, the emission colour of the singly doped phosphor can be tuned by changing the Sr^{2+} content. The highest emission intensity occurs at 0.4 mol% Sr^{2+} that corresponds to white light on CIE, thus suggesting that this kind of novel phosphor can meet the application requirements for white LEDs.

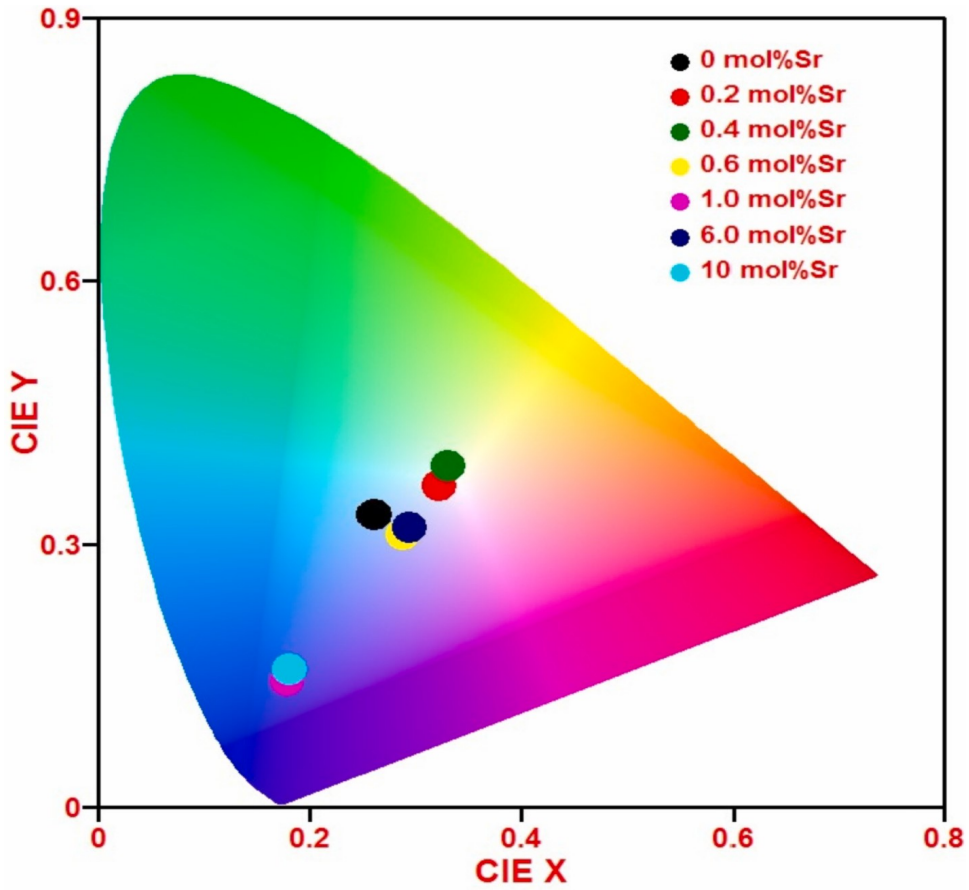

Fig. 3.9: Chromaticity coordinates for the SiO_2:x Sr^{2+} ($0 \leq x \leq 10$ mol% Sr^{2+}) series.

Table 3.1: Sample identification and CIE colour coordinates.

Sample (SiO_2:x mol% Sr^{2+})	CIE (x; y)
x = 0	0.2609; 0.3342
x = 0.2	0.3224; 0.3665
x = 0.4	0.3327; 0.3867
x = 0.6	0.2867; 0.3114
x =1.0	0.1792; 0.1438
x = 6.0	0.2933; 0.3188
x = 10	0.1806; 0.1580

3.4. Conclusion

The SiO_2:x Sr^{2+} phosphors were successfully prepared using the sol- gel method. The XRD results showed that the prepared samples changed from amorphous (SiO_2) to crystalline state with the increase in Sr^{2+} concentration. The presence of Si, Sr and O in the samples was confirmed by the EDS elemental analysis and mapping images. The SEM images show irregular agglomerated particles, with no apparent difference in size with increasing Sr^{2+} concentration, whilst, from TEM results it can be seen that there is structural change from amorphous to crystalline as the Sr^{2+} concentration increases. The PL results indicated the effect of Sr^{2+} concentration on the luminescence of the samples, with maximum intensity experienced at 0.4 mol% Sr^{2+} and quenching as the Sr^{2+} concentration increased further. The CIE analysis showed that the colour coordinates for the x = 0.2 and 0.4 mol% Sr^{2+} well related to white light emission, while varying the Sr^{2+} concentration influenced the emission colour shift.

References

1. B. Moine, G. Bizarri, *Mater. Sci. Eng. B* 105 (2003) 2–7.
2. D. Cervantes-Vasquez, O.E. Contreras, G.A. Hirata, *J. Lumin.* 143 (2013) 226–232.
3. I.P. Sahu, D.P. Bisen, R.K. Tamrakar, *Int. J. Lumin. Appl.* 6 (1) (2016) 25–34.
4. H. Nagabhushana, D.V. Sunitha, S.C. Sharma, B. Daruka Prasad, B.M. Nagabhushana, R.P.S. Chakradhar, *J. Alloy. Comp.* 595 (2014) 192–199.
5. H. Ji, Z. Huang, Z. Xia, M.S. Molokeev, V.V. Atuchin, M. Fang, S. Huang, *Inorg. Chem.* 53 (2014) 5129–5135.
6. J.L. Leano Jr., S. Lin, A. Lazarowska, S. Mahlik, M. Grinberg, C. Liang, W. Zhou, M. S. Molokeev, V.V. Atuchin, Y. Tsai, C.C. Lin, H. Sheu, R. Liu, *Chem. Mater.* 28 (2016) 6822–6825.
7. C. Lorbeer, A.V. Mudring, *J. Phys. Chem. C* 117 (23) (2013) 12229–12238.
8. R.E. Kroon, H.A.A. Seed Ahmed, O.M. Ntwaeaborwa, L.F. Koao, I.M. Nagpure, M. A. Gusowski, J.R. Botha, H.C. Swart, *Physica B* 407 (2012) 1595–1598.
9. R.D. Shannon, *Acta Crystallogr.* A32 (1976) 751–767.
10. N. Rajamanickam, S.S. Kanamni, S. Rajashabala, K. Ramachandran, *Mater. Lett.* 161 (2015) 520–522.
11. N. Wang, W. Zhou, Y. Liang, W. Cui, P. Wu, *J. Mater. Sci. Mater. Electron.* 26 (2015) 7751–7756.
12. S. Lakshmana Perumal, P. Hemalatha, M. Alagara, K. Navaneetha Pandiyaraj, *IJCPS* 4 (2015) 1–13.
13. G.F. Neilson, M.C. Weinberg, *J. Non-Cryst. Solids* 63 (3) (1984) 365–374.
14. S.V. Motloung, F.B. Dejene, H.C. Swart, O.M. Ntwaeaborwa, *Ceram. Int.* 41 (2015) 6776–6783.

15. C.S. Lim, V.V. Atuchin, A.S. Aleksandrovsky, M.S. Molokeev, *Mater. Lett.* 181 (2016) 38–41.

16. C.S. Lim, V. Atuchin, A. Aleksandrovsky, M. Molokeev, A. Oreshonkov, *J. Am. Ceram. Soc.* 98 (10) (2015) 3223–3230.

17. Z.Sh Shaymardanov, S.S. Kurbanov, R. Yu Rakhimov, *Opt. Spectrosc*. 120 (6) (2016) 922–925..

18. R. Reisfeld, A. Patra, G. Panczer, M. Gaft, *Opt. Mater.* 13 (1999) 81–88.

19. Y. Han, J. Lin, H. Zhang, *Mater. Lett.* 54 (2002) 389–396.

20. J.R. Martinez, S. Palomares-Sanchez, G. Ortega-Zarzosa, F. Ruiz, Y. Chumakov, *Mater. Lett.* 60 (2006) 3526–3529.

21. S.K. Gupta, S. Nigam, A.K. Yadav, M. Mohapatra, S.N. Jha, C. Majumder, D. Bhattacharyya, *New J. Chem.* 39 (2015) 6531–6539.

22. M. Jafarzadeh, I.A. Rahman, C.S. Sipaut, *Ceram. Int.* 36 (2010) 333–338.

23. L. Skuja, *J. Non-Cryst. Solids* 239 (1998) 16–48.

24. I.A. Rahman, P. Vejayakumaran, C.S. Sipaut, J. Ismail, C.K. Chee, *Mater. Chem. Phys.* 114 (1) (2009) 328–332.

25. H. He, Y. Wang, H. Tang, *J. Phys. Condens. Matter* 14 (2002) 11867–11874.

26. Z. Wei, P. Yan, W. Feng, J. Dai, Q. Wang, T. Xia, *Mater. Char.* 57 (2006) 176–181.

27. J. Lin, Y. Huang, J. Zhang, J. Gao, X. Ding, Z. Huang, C. Tang, L. Hu, D. Chen, *Chem. Mater.* 19 (10) (2007) 2585–2588.

28. L.F. Koao, Synthesis and Characterization of Cerium Doped Silica Nanophosphors Co-doped with Aluminium or Magnesium Ions, Masters' Thesis, University of the Free State, Qwaqwa, South Africa, 2009.

29. L.F. Koao, H.C. Swart, F.B. Dejene, *J. Rare Earths* 28 (2010) 206–210.

30. A.E. Abbass, H.C. Swart, R.E. Kroon, *J. Lumin.* 160 (2015) 22–26.

31. C. Mbakaan, I. Ahemen, A.N. Amah, A.D. Onojah, L. Koao, *Appl. Phys. A* 124 (741) (2018) 1–9.

Chapter 4 - Morphology, structural and luminescent properties of sol-gel synthesized SiO_2 powders co-doped with Sr^{2+} and Tb^{3+}.

(Published in *Physica B: Condensed Matter,* 580 (2020) 411817)

4.1 Introduction

Phosphors or luminescent materials are mostly solid inorganic materials consisting of a host lattice that is intentionally doped with "impurities", and they have potential applications in modern technologies like lighting and displays [1, 2]. In general, the host material should possess good optical, mechanical and thermal properties [3]. The amorphous SiO_2 prepared by sol-gel technique used as the host lattice in this study because of its chemical and thermal stability, optical inertness, non-hygroscopic nature, the possibility of incorporating larger amounts of luminescent ions and the opportunity of cost reduction [3,4]. The use of glasses synthesized by the sol-gel method in opto-electronics and photonics has opened up the new way for the development of unique information systems with tunable characteristics over a wide frequency range [5]. Whilst, sol-gel was the preferred method of preparation since it is considered as an efficient technique for the synthesis of phosphors due to the good mixing of starting materials and relatively low reaction temperature than the melt process [6].

The RE^{3+} ions based luminescent materials have the following characteristics: their emissions are due to the unique 4f – 4f or 4f – 5d transitions of the RE^{3+}, the emissions have high colour purity due to shielding of 4f electrons by outer 5s and 5p electrons. In addition, the host lattice has little influence on the positions of the 4f configuration energy levels [7,8]. Tb^{3+} is the RE^{3+} used in this study due to its bright green emission [9]. Bae et al. [8] showed that it exhibits strong absorption in the range 240–260 nm that is difficult to access because of the short wavelength. The luminescence efficiency of Tb^{3+} ions can be enhanced through energy transfer

from sensitizer ions whose absorption occur at longer wavelengths that are more accessible. Several researchers [2, 10–12] have found Ce^{3+} ions to be an efficient sensitizer for Tb^{3+} ions when they are co-doped. The explanation for this energy transfer process from Ce^{3+} to Tb^{3+} ions is that the average distance between Tb^{3+} ions in a Tb^{3+} doped shell is shorter than in a co-doped core phosphor; at closer distances a strong interaction is established between Tb^{3+} ions enabling more non radiative cross-relaxation processes [13]. Co-doping enhances luminescence by acting as charge compensator, reducing concentration quenching through lowering the concentration of close activator ions and/or creating as well as affecting the concentration of intrinsic defects [14]. Co-doping of RE^{3+} elements such as Tb^{3+}, Ce^{3+}, Eu^{3+}, Sm^{3+} etc. and energy transfer between these dopants in different host matrices have been reported. For example, Motloung et al. [15] reported the colour tuning and energy transfer pathways in $MgAl_2O_4$ triply doped with 0.1% Ce^{3+}, 0.1% Eu^{2+}, x% Tb^{3+} ($0 \leq x \leq 2\%$) nanocrystals synthesized using sol-gel process. They have observed that the PL results revealed the existence of the energy transfer from $Eu^{2+} \rightarrow Tb^{3+} \rightarrow Ce^{3+}$. Ntwaeaborwa et al. [12] reported on the enhanced luminescence and degradation of SiO_2:Ce^{3+}, Tb^{3+} powder phosphors prepared by a sol-gel process. They have realized enhanced green PL from Tb^{3+} ions due to co-doping with Ce^{3+} ions from SiO_2:Ce, Tb powder phosphors prepared by a sol-gel technique. Blue emission from the Ce^{3+} ions was completely suppressed by Tb co-doping, presumably due to energy transfer from $Ce^{3+} \rightarrow Tb^{3+}$ [12]. Ahmed et al. [16] reported on high efficiency energy transfer in Ce^{3+}, Tb^{3+} co-doped silica prepared by sol-gel method. They found very efficient energy transfer from Ce to Tb was achieved if the samples were annealed in a reducing environment to facilitate the formation of Ce^{3+} rather than Ce^{4+} ions.

There is however in our knowledge no report on the co-doping of SiO_2 with Tb^{3+} and Sr^{2+}. Thus, in this study, a series of SiO_2 doped with 0.4 mol% Sr^{2+} and co-doped with different x mol% of Tb^{3+} (where x = 0.04, 0.08, 0.1, 0.4 and 0.5) was synthesized using sol-gel method.

All the samples were annealed under N_2 at 800 ^{0}C for 2 h. The proposed energy transfer mechanism from $SiO_2 \rightarrow Tb^{3+}$ and emission pathways are also presented. The structural, morphological and optical properties of the prepared samples are discussed in details. This investigation contributes a new body of knowledge on the development of new potential and alternative phosphor materials for practical application such as in lighting emitting technology.

4.2 Experimental

The sol-gel synthesis was carried out as reported elsewhere [17, 18]. SiO_2 was prepared using 99% tetraorthosilicate ($Si(OC_2H_5)_4$, TEOS), 95% ethanol (C_2H_5OH, EtOH), nitric acid (HNO_3) all of which were analytic grade and distilled water. TEOS (10 mL) and EtOH (10 mL) were combined and stirred for about 30 min. Then HNO_3 (5 mL) and distilled water (14 mL) were added to the solution and the mixture was stirred at room temperature until gel point. The volume ratio of TEOS: ETOH: H_2O: HNO_3 was kept constant at 1:1:1.4:0.5. However, in synthesizing Sr^{2+} and Tb^{3+} co-doped SiO_2, the SiO_2 solution was stirred for 1 h. Thereafter, strontium acetate (0.4 mol% $Sr2^{+}$) and various amounts of terbium acetate, previously dissolved in 5 mL of ethanol were added to the SiO_2 solution and the mixture was further stirred until gel point. The amounts terbium acetate in this study were varied to give the following concentrations of Tb^{3+}: 0.04, 0.08, 0.1, 0.4 and 0.5 mol%. The gels were then dried in air at room temperature for approximately 24 h. The air-dried gels were then crushed to fine powder and heat treated at 100 ^{0}C for 2 h to remove solvent and organic ligands and in order to obtain full densification. The powders were re-crushed, and annealed at 800 ^{0}C for 2 h under nitrogen atmosphere. The powders were further crushed using the mortar and pestle and packaged for characterization with different techniques. The structures of the samples were determined with a Bruker AXS Discover diffractometer with Cu-Kα (1.54 Å) radiation. The morphology of the prepared nanoparticles was determined with a scanning electron microscopy (SEM) using a

Shimadzu model ZU SSX-550 Superscan coupled with an energy dispersive X-ray spectrometer (EDS) and Zeiss Supra 55-VP. Diffuse reflectance measurements were carried out in the 200–800 nm wavelength range using a PerkinElmer UV/Vis Lambda 950 Spectrophotometer. Photoluminescence measurements were done with a 325 nm He–Cd laser PL system.

4.3 Results and discussion

4.3.1 Structural and compositional analysis

Fig. 4.1 (a) shows the XRD results of SiO_2 and SiO_2:0.4 mol% Sr^{2+}: x mol% Tb^{3+} (where x = 0, 0.04, 0.08, 0.1, 0.4 and 0.5) annealed at 800 ºC under nitrogen atmosphere. All the samples exhibited broad peaks at around 2θ = 22º - 25º, which corresponds to the characteristic diffraction peak of pure amorphous SiO_2, indicating that no other phases or impurities were formed [7, 19]. The peak intensity slightly increases with Sr^{2+} doping and Tb^{3+} co-doping compared to SiO_2 (host) as shown in Fig. 4.1 (b). The change on the diffraction peak intensity indicates that the structure of the samples depends on the Sr^{2+} and Tb^{3+} concentration [20]. The decrease in peak intensity observed above SiO_2:0.4 mol% Sr^{2+}: 0.08 mol% Tb^{3+} may be due to the incorporation of Tb^{3+} ions into the network structure of SiO_2 rather than the substitution of Si^{4+} by Tb^{3+} since the difference in their ionic radii is large (0.26 Å and 1.04 Å, respectively) [7]. There is also a slight shift in the position of the peak to higher diffraction angles for all the co-doped samples, which confirms the incorporation of the Tb^{3+} into the structure of SiO_2 [21].

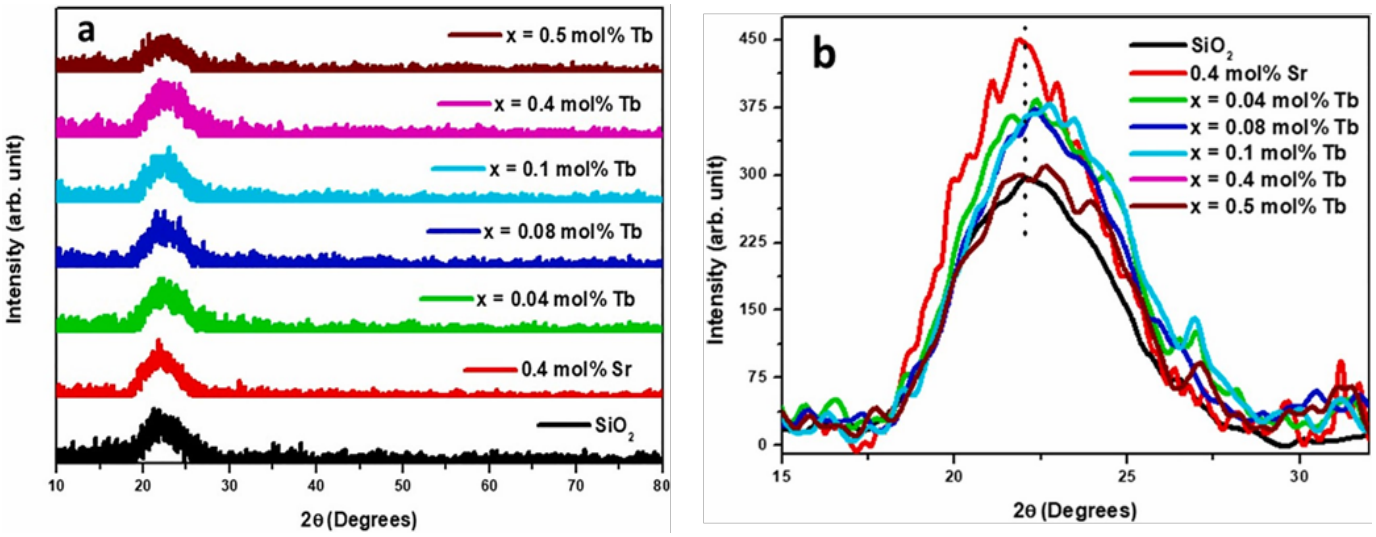

Fig. 4.1: (a) X-ray powder diffraction patterns for the SiO_2 (host), SiO_2:0.4 mol% Sr^{2+}: x mol% Tb^{3+} (where x = 0, 0.04, 0.08, 0.1, 0.4 and 0.5) samples and (b) analysis of the diffraction peak.

Fig. 4.2 depicts the SEM images of the prepared nanopowder of the SiO_2, singly doped and co-doped samples. Fig. 4.2 (a) and (b) shows the SiO_2 and singly doped samples, which illustrate a rough surface with spherical and agglomerated particles. In-comparison to the un-doped sample in Fig. 4.2 (a) the results in Fig. 4.2 (b) show that Sr^{2+} doping does not influence the shape. Fig. 4.2 (c–e) depict the microstructure of the co-doped samples, and shows agglomerated spherical nanoparticles. It is clear that the introduction of co-dopants into SiO_2 does not result in a significant change in the shape of the nanoparticles. This is in agreement with the XRD results presented in Fig. 4.1 when taking into account that doping and co-doping did not changed the structure of undoped SiO_2. From Fig. 4.2 (a–e) it can be noted that particles size have increased slightly in singly doped and co-doped samples compared to the undoped which agrees very well

with the observed increase in XRD peak intensity. Hence, it can be concluded that doping and co-doping do not influence the shape but slightly influences the particle size.

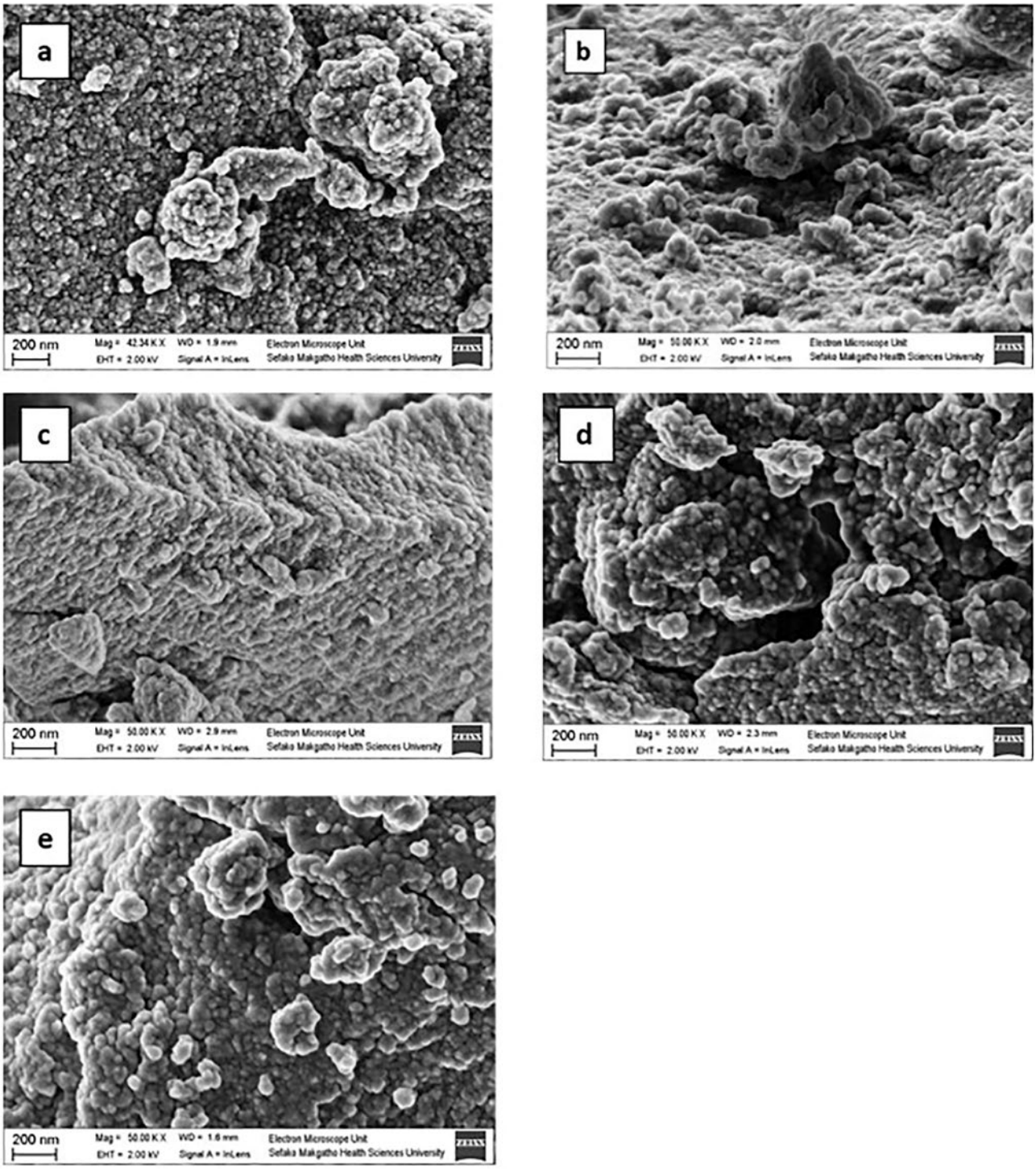

Fig. 4.2: SEM images for (a) SiO_2 and SiO_2:0.4 mol% Sr^{2+}: x mol% Tb^{3+} (b) x = 0 (c) x = 0.04 (d) x = 0.1 (e) x = 0.5.

The EDS spectra for the samples SiO_2:0.4 mol% Sr^{2+}: x mol% Tb^{3+} (where x = 0.04 and 0.5 respectively) are respectively shown in Fig. 4.3. Both Fig. 4.3 (a) and (b) confirm the existence of the Si, O, Sr, Tb and carbon (C) peaks. The C peak is due to the conductive carbon films coated on the sample holders during the course of the EDS measurement. Apart from the anticipated elements, there were no other peaks that were detected, which agrees very well with the XRD results in Fig. 4.1 (a).

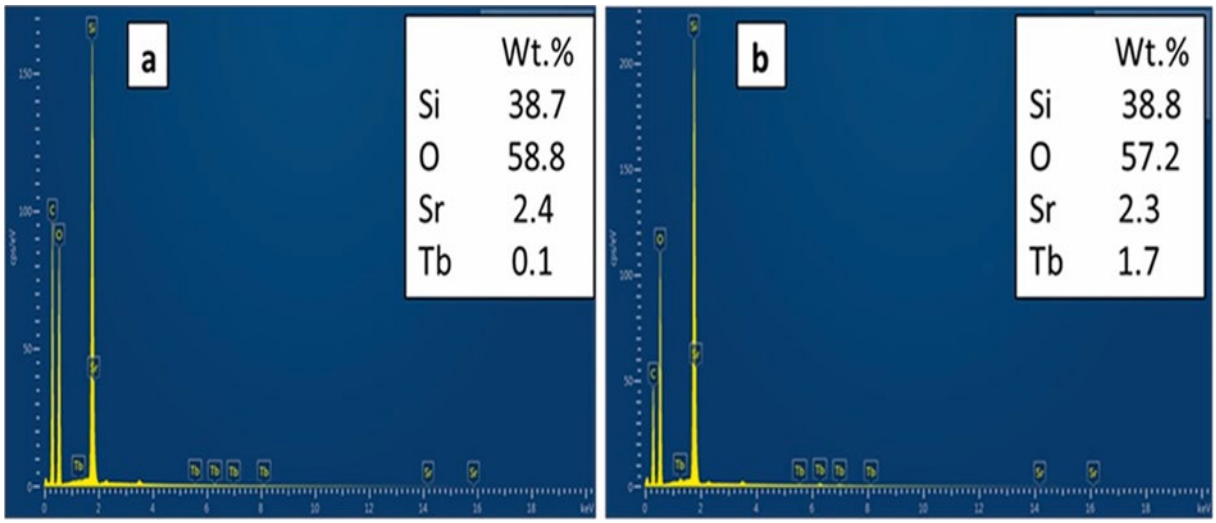

Fig. 4.3: EDS spectra for the SiO_2:0.4 mol% Sr^{2+}: x mol% Tb^{3+} (a) x = 0.04 and (b) x = 0.5.

Fig. 4.4 (a) and (b) shows the elemental distribution on the surface of the samples as measured by EDS. The EDS elemental maps confirm the homogeneous distribution of the anticipated elements for the chosen samples.

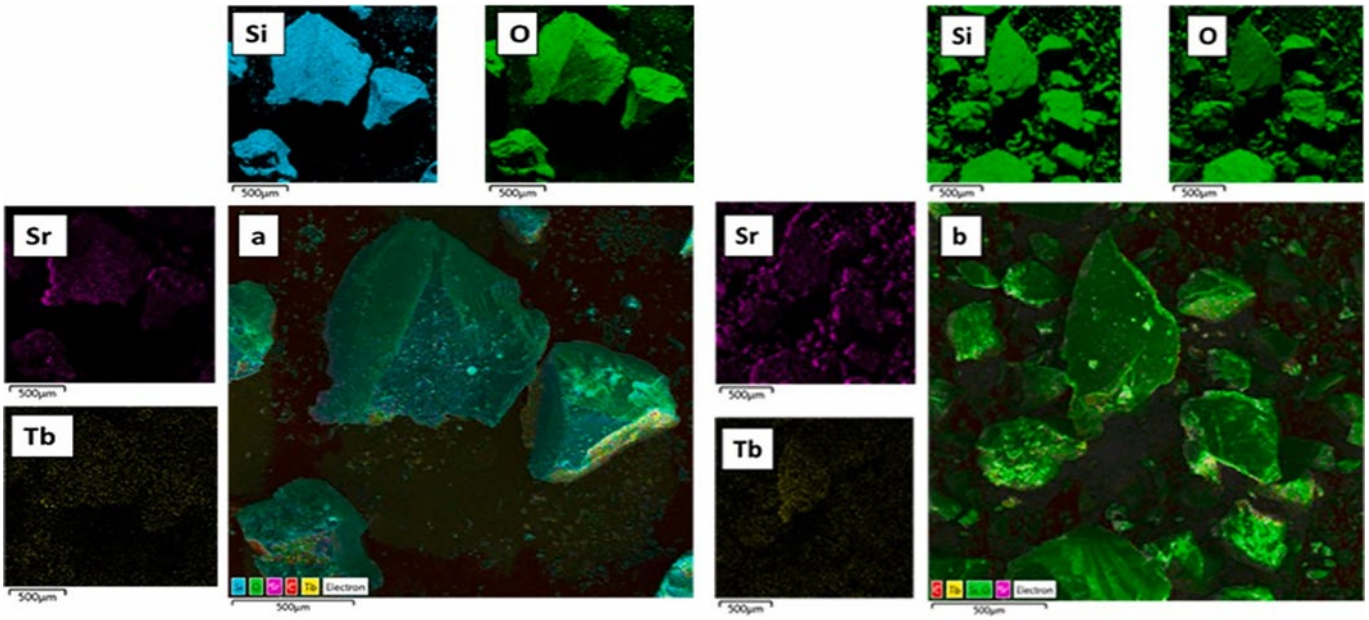

Fig. 4.4: Elemental maps for the SiO_2:0.4 mol% Sr^{2+}: x mol% Tb^{3+} (a) x = 0.04 (b) x= 0.5.

4.3.2 Ultraviolet–visible (UV–vis) spectroscopy

The diffuse reflectance spectra of the SiO_2 and SiO_2:0.4 mol% Sr^{2+}: x mol% Tb^{3+} (where x = 0, 0.04, 0.08, 0.1, 0.4 and 0.5) is shown in Fig. 4.5 (a). The figure shows clearly that the absorption edge at around 400 nm (from the host) shifts to around 365 nm for both the singly doped and co-doped samples. The observed shift of absorption edge to lower wavelength may be due the alteration of the defects induced by the dopants. The band gap of the host, singly doped and co-doped samples were estimated using the relationship between the Kubelka-Munk relationship, and Wood and Tauc relation [22]. Fig. 4.5 (b) illustrates the Kubelka-Munk function $K = (1 - R)^2/2R$ used to transform the reflectance to the values proportional to absorbance [23]. The Tauc plot of $(K \times h\nu)^n$ against $h\nu$ is presented in Fig. 4.5 (b), where $h\nu$ is the incident photon energy, n is the exponent that determines the type of electronic transition causing the absorption that can take the values 1/2 or 2 depending whether the transition is indirect or direct [24]. In this study, n was chosen to be 1/2 because SiO_2 is an indirect band gap material. The band gap energy of the SiO_2 increases from 3.11 to 3.41 eV due to the

introduction of Sr^{2+}. On the other hand, the introduction of Tb^{3+} co-dopant results in the initial increase of the estimated band gap from 3.41 eV for the singly doped sample to 3.84 eV for 0.04 mol% Tb^{3+}. There is an increase in the band gap to 3.93 eV for the co-doped samples for Tb^{3+} concentration up to 0.1 mol% and then a subsequent decrease to 3.67 eV for Tb^{3+} concentration up to 0.5 mol%. Other researchers [25–27] determined that the band gap of SiO_2 could vary from 3.15 to 4.49 eV, which is within the estimated band gap in this study. The observed increase in band gap may be due to the change in the porosity and surface area of the sample [27].

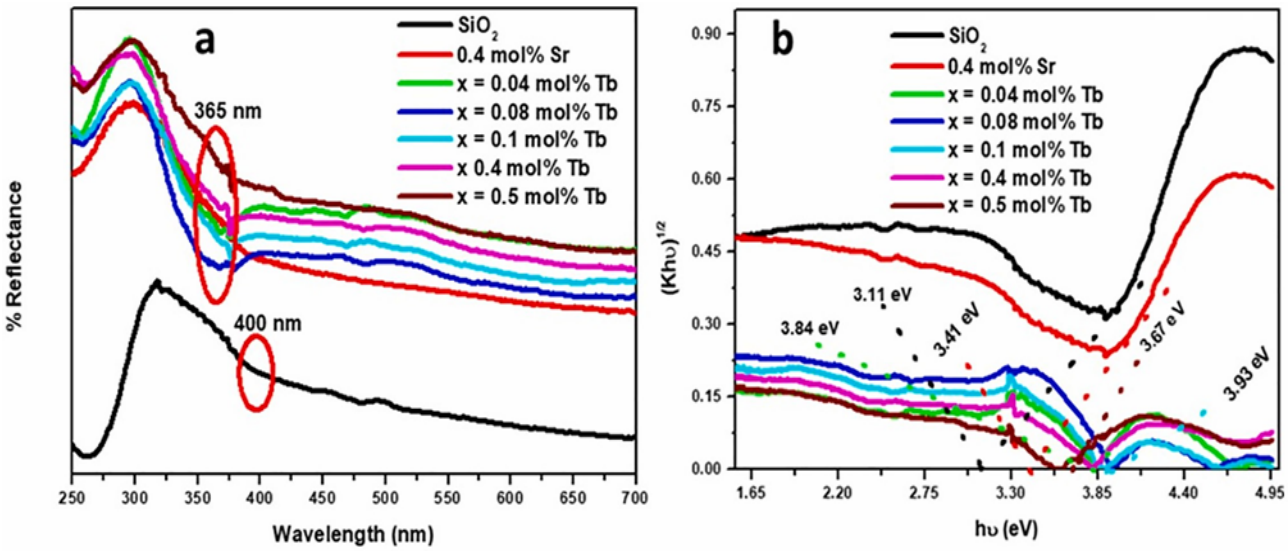

Fig. 4.5: (a) Diffuse reflectance spectra of the SiO_2 (host) and SiO_2:0.4 mol% Sr^{2+}: x mol% Tb^{3+} series and (b) optical band gap estimation.

4.3.3 Photoluminescence (PL)

The PL emission spectra of SiO_2, SiO_2:0.4 mol% Sr^{2+} and SiO_2:0.4 mol% Sr^{2+}: x mol% Tb^{3+} (where x = 0.04, 0.08, 0.1, 0.4 and 0.5) excited with He–Cd laser at 325 nm in ambient temperature are shown in Fig. 4.6 (a). It is clear that the Sr^{2+}- doped and Tb^{3+}-co-doped have effect on both luminescence intensity and wavelength compared to undoped SiO_2. In order to

explore the origin of each emission peak observed in Fig. 4.6 (a), the normalized emission spectra is depicted in Fig. 4.6 (b). The results clearly show that the SiO_2 has a broad emission peak with a maximum at around 415 nm. The Sr^{2+}- doped sample shows additional peaks at 490 and 544 nm. All of these emission peaks are due to the defects within SiO_2 [28, 29]. Therefore, it is clear that doping with Sr^{2+} stimulates both 490 and 544 nm emissions from the SiO_2. Some authors [28, 29] relate the peaks at around 490 and 544 nm in greenish region to the presence of hydrogen related species. From Fig. 4.6 (a) it can also be seen that the presence of Tb^{3+} ions affect the emission wavelength and intensity. The luminescence bands of Sr^{2+} doped SiO_2 at around 490 and 544 nm diminish with an increase in the concentration of Tb^{3+}, while those due to Tb^{3+} emerge with an increase in the molar concentration of Tb^{3+} ions. This behaviour may be due to a well-known energy transfer from SiO_2 defects emission to Tb^{3+} ions [12, 30, 31]. The Tb^{3+} co-doped samples show emission peaks centred at 415, 487, 541, 550, 585 and 622 nm, which are attributed to the $^5D_3 - {}^7F_5$ and $^5D_4 - {}^7F_J$ (J = 6, 5, 4, 3), respectively [12]. Fig. 4.6 (c) depicts the relation between emission intensity and the concentration of Tb^{3+} at various wavelengths. It can be observed that the peak at 415 nm, which is from both the host and Tb^{3+}, increases with the concentration of Tb^{3+} and reaches a maximum at 0.1 mol% Tb^{3+}. While, the most prominent Tb^{3+} peak around 541 nm (which is similar to the other researchers [12, 32]) increases with an increase in Tb^{3+} and reaches a maximum at 0.4 mol% Tb^{3+}. This decrease in intensity may be attributed to the phenomenon of cross relaxation (concentration quenching) and non-radiative relaxation [10, 32]. The improved intensity of the blue to green emission in this study may be due to the increase in the activator (Tb^{3+}) ions.

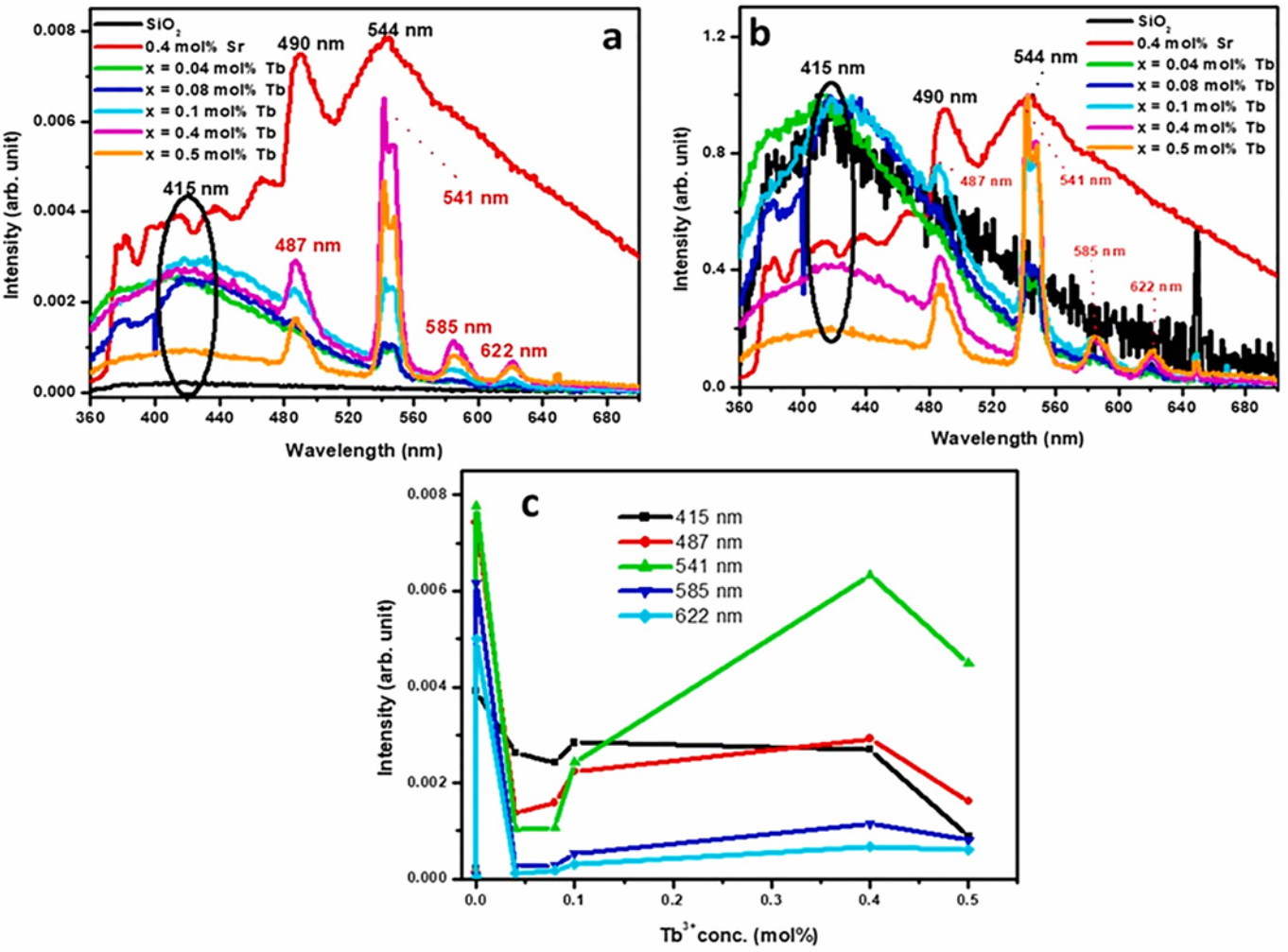

Fig. 4.6: (a) PL emission spectra (b) normalized PL emission spectra of SiO_2 (host) and SiO_2:0.4 mol% Sr^{2+}: x mol% Tb^{3+} (where x = 0, 0.04, 0.08, 0.1, 0.4 and 0.5) and (c) Intensity as a function of Tb^{3+} concentration at various wavelengths.

Fig. 4.7 (a) – (c) illustrates the proposed luminescence mechanisms for the observed emissions. The observed increase in the emission intensity of the Tb^{3+} dopant at the expense of the emission from defect states of the host confirms the energy transfer from the defects states of SiO_2 to the Tb^{3+} ion [22].

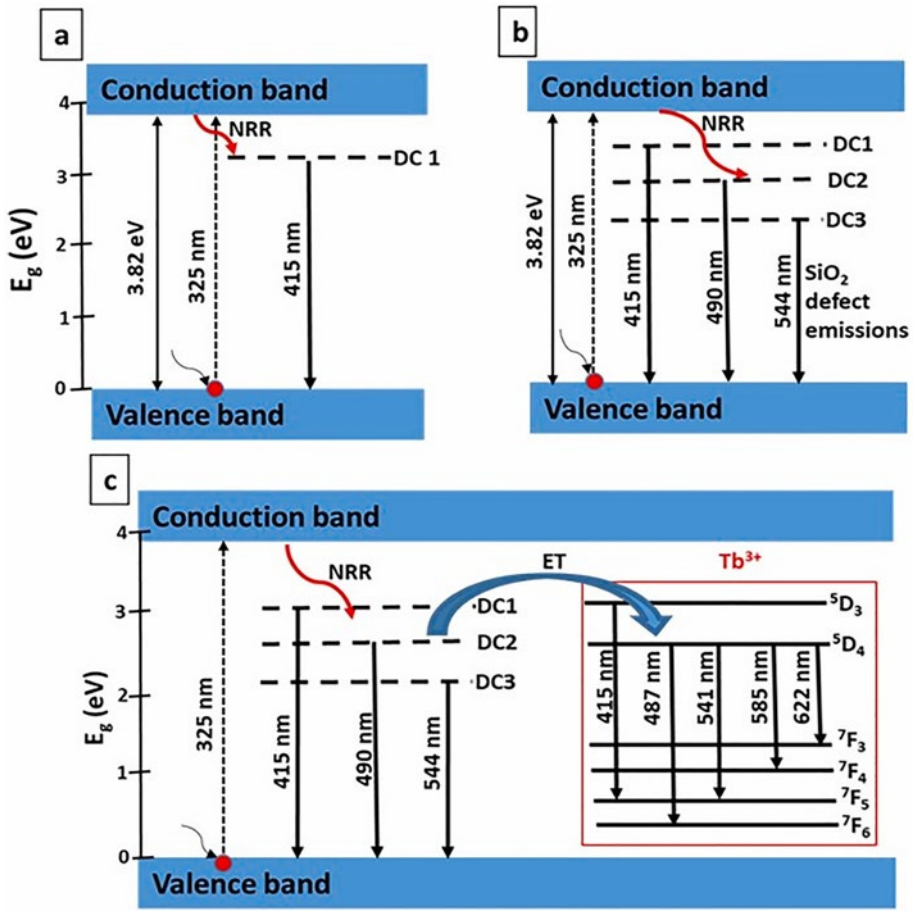

Fig. 4.7: The proposed emission pathways mechanism for (a) SiO_2 (host), (b) SiO_2: 0.4 mol% Sr^{2+} and (c) SiO_2:0.4 mol% Sr^{2+}: x mol Tb^{3+} (where x = 0.04, 0.08, 0.1, 0.4 and 0.5).

Fig. 4.8 displays the Commission Internationale de l'Eclairage (CIE) colour chromaticity diagrams for the SiO_2 (host) and co-doped samples of SiO_2:Sr^{2+}:Tb^{3+}, the samples are identified in Table 4.1. The CIE colour coordinates were calculated using the CIE coordinate calculator software. The results showed that the colour changes from blue to green with an increase in the concentration of Tb^{3+}. Thus, the emission of the SiO_2:0.4 mol% Sr^{2+}: x mol% Tb^{3+} (where x = 0.04, 0.08, 0.1, 0.4 and 0.5) can be tuned by varying the concentration of Tb^{3+}. More interestingly, the CIE analysis showed that the colour for the 0.4 mol% Sr^{2+} gave white light emission. Hence, we conclude that the emission colour can be tuned by varying both the

concentration of Sr^{2+}- doped and Tb^{3+}-co-doped which suggests that this kind of novel phosphor can meet the wide range of application requirements such in blue to green LEDs.

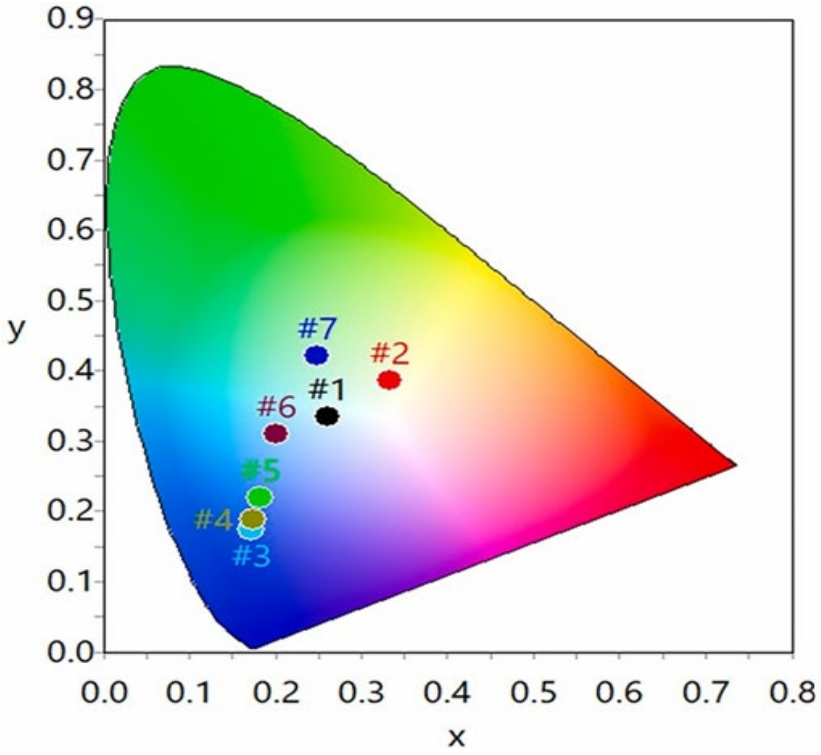

Fig. 4.8: Chromaticity coordinates for the host and SiO_2:0.4 mol% Sr^{2+}: x mol% Tb^{3+} (where x = 0, 0.04, 0.08, 0.1, 0.4 and 0.5).

Table 4.1: Summary of sample identification and CIE colour coordinates.

Sample number	Sample identification	CIE (x;y)
#1	SiO_2	0.2609; 0.3342
#2	SiO_2:0.4 mol% Sr^{2+}	0.3327; 0.3867
#3	SiO_2:0.4 mol% Sr^{2+}: 0.04 mol% Tb^{3+}	0.1729; 0.1746
#4	SiO_2:0.4 mol% Sr^{2+}: 0.08 mol% Tb^{3+}	0.1751; 0.1893
#5	SiO_2:0.4 mol% Sr^{2+}: 0.1 mol% Tb^{3+}	0.1829; 0.2186
#6	SiO_2:0.4 mol% Sr^{2+}: 0.4 mol% Tb^{3+}	0.2014; 0.3100

4.4 Conclusion

A series of SiO_2, SiO_2:0.4 mol% Sr^{2+} singly doped and SiO_2:0.4 mol% Sr^{2+}: x mol% Tb^{3+} (where x = 0.04, 0.08, 0.1, 0.4 and 0.5) co-doped phosphors was successfully prepared. The XRD analysis showed that all the samples were amorphous with a broad diffraction peak associated with amorphous SiO_2. SEM depicted that doping and co-doping did not have any significant influence on the host particle shape, while EDS confirmed the elemental composition of the samples. The PL emission spectra showed emission peaks from both the SiO_2 and Tb^{3+}. The SiO_2 emission peaks at 490 and 544 nm were activated or stimulated by Sr^{2+} doping. The energy transfer was observed from the SiO_2 to Tb^{3+}.The addition of Tb^{3+} can tune the colour of the phosphors from blue to green as shown by the CIE colour chromaticity.

References

1. C.R. Ronda, T. Justel, H. Nikol, *J. Alloy. Comp.* 275 (1998) 669–676.

2. H.A.A. Seed Ahmed, A. Yousif, H.C. Swart, R.E. Kroon, *Mater. Today: Proc.* 2 (2015) 4111–4117.

3. H.A.A. Seed Ahmed, O.M. Ntwaeaborwa, R.E. Kroon, *J. Lumin.* 135 (2013) 15–19.

4. R.E. Kroon, H.A.A. Seed Ahmed, O.M. Ntwaeaborwa, L.F. Koao, I.M. Nagpure, M. A. Gusowski, J.R. Botha, H.C. Swart, *Physica B* 407 (2012) 1595–1598.

5. N.N. Khimich, G.M. Berdichevskii, E.N. Poddenezhnyi, V.V. Golubkov, A.A. Boiko, V.M. Ken'ko, O.B. Evreinov, L.A. Koptelova, *Glass Phys. Chem.* 33 (2) (2007) 152–155.

6. J.M. Nedelec, L. Courtheoux, E. Jallot, C. Kinowski, J. Lao, P. Laquerriere, C. Mansuy, G. Renaudin, S. Turrell, *J. Sol. Gel Sci. Technol.* 46 (2008) 259–271.

7. J.A. Gonzalez-Ortega, E.M. Tejeda, N. Perea, G.A. Hirata, E.J. Bosze, J. McKittrick, *Opt. Mater.* 27 (2005) 1221–1227.

8. D.S. Bae, K.J. Jeong, *15th Eur. Conf. on Comp. Mater.* (2012) 1.

9. M. M.A. Abualrejal, H. Zou, J. Chen, Y. Song, Ye Sheng, *Adv. Nanoparticles* 6 (2017) 11–21.

10. D. Jiang, J. Wen, M. Jia, Q. Guo, Z. Xiao, W. Luo, F. Pang, Z. Chen, T. Wang, *Opt. Mater. Express* 8 (6) (2018) 1593–1602.

11. S. Gutzov, M. Bredol, *J. Mater. Sci.* 141 (2006) 1835–1837.

12. O.M. Ntwaeaborwa, H.C. Swart, R.E. Kroon, P.H. Holloway, J.R. Botha, *J. Phys. Chem. Solids* 67 (2006) 1749–1753.

13. D. Cervantes-Vasquez, O.E. Contreras, G.A. Hirata, *J. Lumin.* 143 (2013) 226–232.

14. L. Borkovska, L. Khomenkova, I. Markevich, M. Osipyonok, T. Stara, O. Gudymenko, V. Kladko, M. Baran, S. Lavoryk, X. Portier, T. Kryshtab, *J. Mater. Sci. Mater. Electron.* 29 (2018) 15613–15620.

15. S.V. Motloung, B.F. Dejene, O.M. Ntwaeaborwa, H.C. Swart, R.E. Kroon, *Chem. Phys.* 487 (2017) 75–86..

16. H.A.A. Seed Ahmed, O.M. Ntwaeaborwa, R.E. Kroon, *J. Lumin.* 135 (2013) 15–19.

17. S.V. Motloung, F.B. Dejene, H.C. Swart, O.M. Ntwaeaborwa, *Ceram. Int.* 41 (2015) 6776–6783.

18. L.F. Koao, H.C. Swart, E. Coetsee, M.M. Biggs, F.B. Dejene, *Physica B* 404 (22) (2009) 4499–4503.

19. H.A.A. Seed Ahmed, O.M. Ntwaeaborwa, M.A. Gusowski, J.R. Botha, R.E. Kroon, *Physica B* 407 (2012) 1653–1655.

20. L.F. Koao, F.B. Dejene, M. Tsega, H.C. Swart, *Physica B* 480 (2016) 53–57.

21. R.E.M. Khaidir, Y.W. Fen, M.H.M. Zaid, K.A. Matori, N.A.S. Omar, M.F. Annnar, S. A.A. Wahab, A.Z.K. Azman, *Respir. Physiol.* 15 (2019) 102596.

22. I. Ahemen, F.B. Dejene, *Curr. Appl. Phys.* 18 (2018) 1359–1367.

23. L.F. Koao, F.B. Dejene, H.C. Swart, J.R. Botha, *J. Lumin.* 143 (2013) 463–468.

24. N. Saha, A. Sarkar, A.B. Ghosh, A.K. Dutta, G.R. Bhadu, P. Paul, B. Adhikary, *RSC Adv.* 108 (2015) 88848–88856.

25. L.H. Gaaboura, *J. Mater. Res. Technol* 8 (2) (2019) 2157–2163.

26. A. Belahmar, A. Chouiyakh, *J. Nanosci. Tech.* 2 (2) (2016) 81–84.

27. E.A.G. Engku Ali, K.A. Matori, E. Saion, H.A.A. Sidek, M.H.M. Zaid, I.M. Alibe, *Dig. J. Nanomater. Biostrs.* 12 (2) (2017) 441–447.

28. Y. Han, J. Lin, H. Zhang, *Mater. Lett.* 54 (2002) 389–396.

29. M. Jafarzadeh, I.A. Rahman, C.S. Sipaut, *Ceram. Int.* 36 (2010) 333–338.

30. S. Bayan, U. Das, D. Mohanta, *Phys. Status Solidi A* 207 (8) (2010) 1859–1863.

31. L.F. Koao, H.C. Swart, F.B. Dejene, *J. Rare Earths* 28 (2010) 206–210.

32. R. Sreeja Sreedharan, R. Reshmi Krishnan, R. Jolly Bose, V.S. Kavitha, S. Suresh, R. Vinodkumar, S.K. Sudheer, V.P. Mahadevan Pillai, *J. Lumin*. 184 (2017) 273–286.

Chapter 5: Characterization of SiO_2 co-doped with Sr^{2+} and Tb^{3+} phosphors immobilized in PLA.

5.1 Introduction

Research on light emitting polymers have a long history and can be classified into mainly three paths, namely, active organic dye doped materials, electroluminescent polymers and polymers doped with RE^{3+} compounds [1]. RE^{3+} ion doped nanoparticles dispersed in a transparent polymer medium are of special interest as potential optoelctronic materials that may find applications as light emitting diodes (LEDs), photonic circuits, full-color displays and chemosensors [2, 3]. These composites are characterized by high luminescence in combination with good physico-mechanical characteristic of the polymer [3]. The immobilization of the phosphor particles in a polymer matrix helps to overcome the problem of emitter layer thickness and thus the reproducibility of the emitted light experienced when phosphors are immobilized in glues such as polyurethane or epoxy resin [3].

Several methods have been used to prepare luminescent polymer composites such as the *in situ* synthesis of luminescent particles within a polymer matrix, direct mixing of phosphor with a polymer solution, mixing with a monomer followed by *in situ* polymerization or melt processing [4 - 8]. Melt mixing followed by extrusion or melt press is a popular technique since it allows all kinds of polymers to form composites which otherwise are difficult to process by other techniques [9].

Biodegradable and renewable polymers have gained considerable attention due to the heightened demand in reducing environmental pollution [1, 10]. Poly(lactic acid) PLA one of the synthetic aliphatic polyester polymers is said to be an attractive alternative to traditional petrochemical polymers such as polystyrene, poly(ethylene terephthalate), polyethylene, poly(vinyl chloride) [11 - 13]. It is characterized by excellent optical properties, high tensile

strength and compostability, but unfortunately, it has relatively poor mechanical properties, low thermal stability and it is rigid and brittle [11, 13, 14].

While SiO_2 can be considered as one of the best filler candidates for preparing polymer composites because of its low cost, high thermal resistance and surface functionalizability [15, 16]. To the best of our knowledge, little work has been reported on PLA composites incorporating SiO_2 nanoparticles as a filler [14, 17, 18, 19]. Therefore, this study focuses on the possibility of engineering the luminescence and influencing the physical, chemical and optoelectronic properties of the PLA by varying the composition of the nanopowders. In particular, the effect of incorporating the SiO_2 doped and co-doped with Sr^{2+} and Tb^{3+} phosphor into PLA have not been reported in literature to date. Thus, the objective of this study was to prepare PLA composites incorporating SiO_2 based phosphors that could emit visible light and can be used in optical detectors, textiles and vivo imaging.

5.2 Experimental

The PLA used in this study was a commercial grade (PLA2002D), obtained from Nature works, LLC (USA). The SiO_2 based phosphors were prepared through the sol-gel technique [20 - 23]. The composites were prepared via melt-mixing [24] using a Brabender Platograph. PLA was dried in an oven at 80 $^{\circ}$C for four hours before mixing and the SiO_2 phosphors were used as prepared. Pure PLA and its composites with 1 wt% of SiO_2 phosphors were mixed at 170 ºC for ten minutes at a speed of 50 rpm. The samples were then compression moulded into 2 mm thick sheets at 170 ºC for five minutes using a hydraulic press at a pressure of fifty bar.

The structural properties of the samples were observed with a Bruker AXS Discover diffractometer with Cu Kα (1.54 Å) radiation. The morphology of the prepared nanoparticles was determined with a Zeiss SUPRA 55-VP scanning electron microscope (SEM). Transmission electron microscopy (TEM) observation was performed with JEOL JEM 2100

transmission electron microscope. The effect of the filler particles on the thermal transitions of the PLA matrix was studied using differential scanning calorimetry (DSC) Perkin Elmer DSC 6000 and the thermogrametric analysis (TGA) Perkin Elmer TGA7 was used to determine the thermal stability of the composites. The diffuse reflectance measurements were carried out in the 200–800 nm wavelength range using a PerkinElmer UV–vis Lambda 950 spectrophotometer. The photoluminescence (PL) measurements were done with a 325 nm He–Cd laser system.

5.3 Results and Discussion

Table 5.1 gives the full identification of the samples as used in the results that follow.

Table 5.1: Sample identification

Abbreviation	Sample identification
PLA	Pure PLA
PLA:Tb0	PLA:SiO_2:0.4mol%Sr^{2+}
PLA:Tb1	PLA:SiO_2:0.4mol%Sr^{2+}:0.02mol%Tb^{3+}
PLA:Tb3	PLA:SiO_2:0.4mol%Sr^{2+}:0.06mol%Tb^{3+}
PLA:Tb5	PLA:SiO_2:0.4mol%Sr^{2+}:0.1mol%Tb^{3+}
PLA:Tb7	PLA:SiO_2:0.4mol%Sr^{2+}:0.3mol%Tb^{3+}
PLA:Tb9	PLA:SiO_2:0.4mol%Sr^{2+}:0.4mol%Tb^{3+}
PLA:Tb10	PLA:SiO_2:0.4mol%Sr^{2+}:0.5mol%Tb^{3+}

5.3.1 Structural and compositional analysis

Fig. 5.1 illustrates the XRD patterns of PLA and the composites. The PLA XRD pattern depicts a wide diffraction peak from 10 - 25º, which is caused by the scattering of PLA polymer matrix [11] and a less intense but still wide peak from 30 - 36º. The XRD patterns for composites

PLA/SiO_2:0.4mol% Sr^{2+}:x mol% Tb^{3+} (where x = 0, 0.02 and 0.06) are closely related to the PLA pattern. While, the XRD patterns for composites PLA/SiO_2:0.4mol% Sr^{2+}:x mol% Tb^{3+} (with $x \geq 0.1$) show a small peak at 13º and a broad diffraction from 32 - 55º. This difference in diffraction pattern between the composites and PLA needs further investigation.

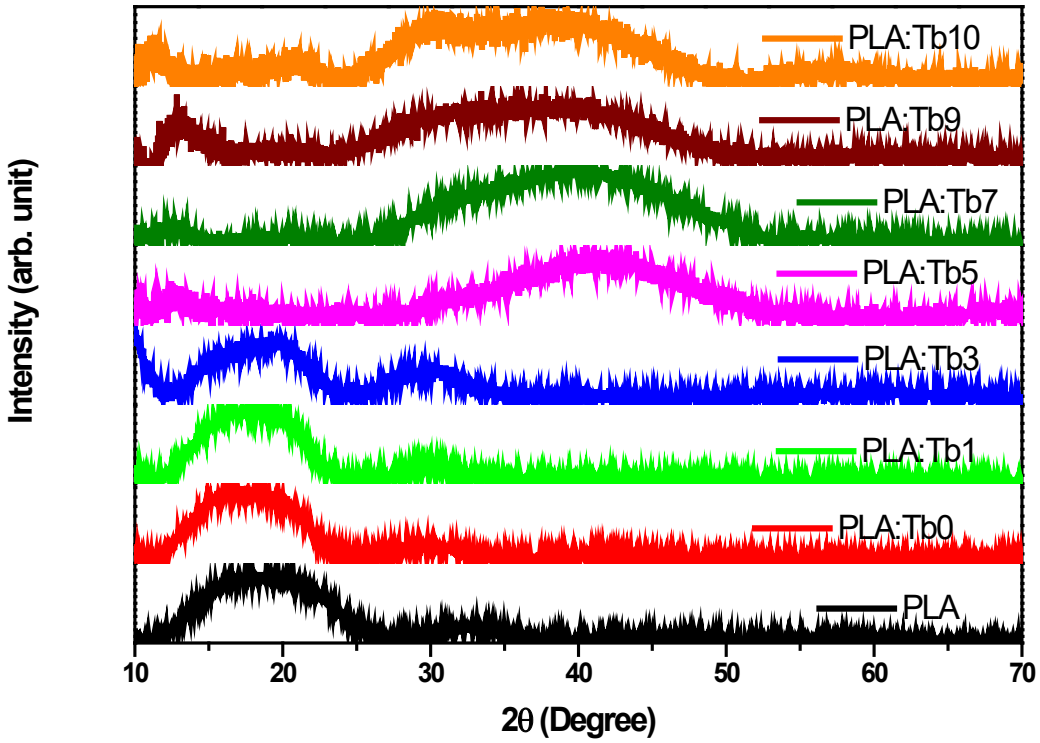

Fig. 5.1: XRD patterns of PLA and PLA/SiO_2:0.4mol%Sr^{2+}:x mol% Tb^{3+} (with $0 \leq x \leq 0.5$) composites.

Fig. 5.2 shows the SEM images of the fractured PLA and its composites. There is no significant change in the morphology of the samples with the introduction of the phosphors and no images show any SiO_2 phosphor particles that support XRD results. This observation may be due to the filler particles not being homogeneously distributed within the polymer matrix.

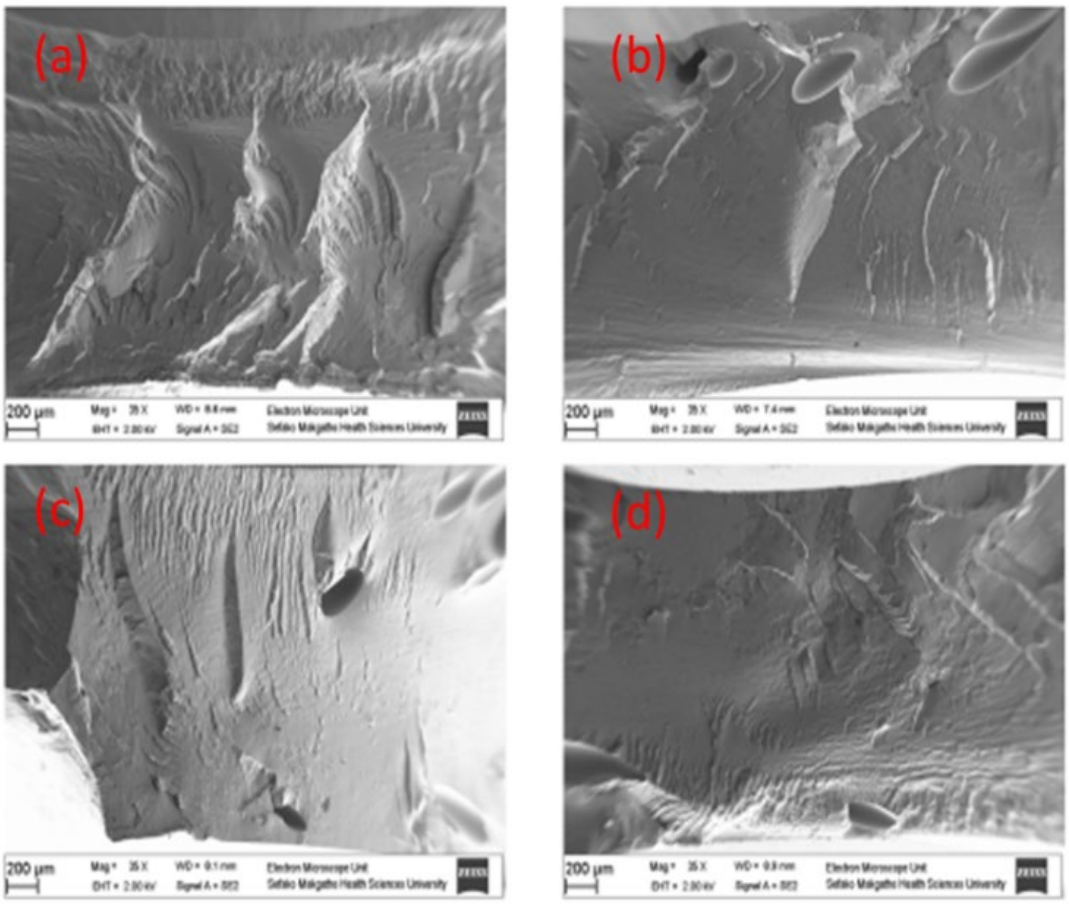

Fig. 5.2: SEM micrographs of (a) PLA, PLA/SiO_2:0.4mol% Sr^{2+}:x mol% Tb^{3+} composites (b) x = 0, (c) x = 0.1 and x = 0.5.

The TEM images for the PLA matrix and the prepared composites are shown in Fig. 5.3. The images show darker patches with the introduction of the doped SiO_2 nanopowder filler that indicate the agglomeration of the filler particles. This observed agglomeration of the phosphor particles in the polymer matrix may hinder the envisaged application of the composites, since there are parts of the polymer matrix that may not have the filler particles .

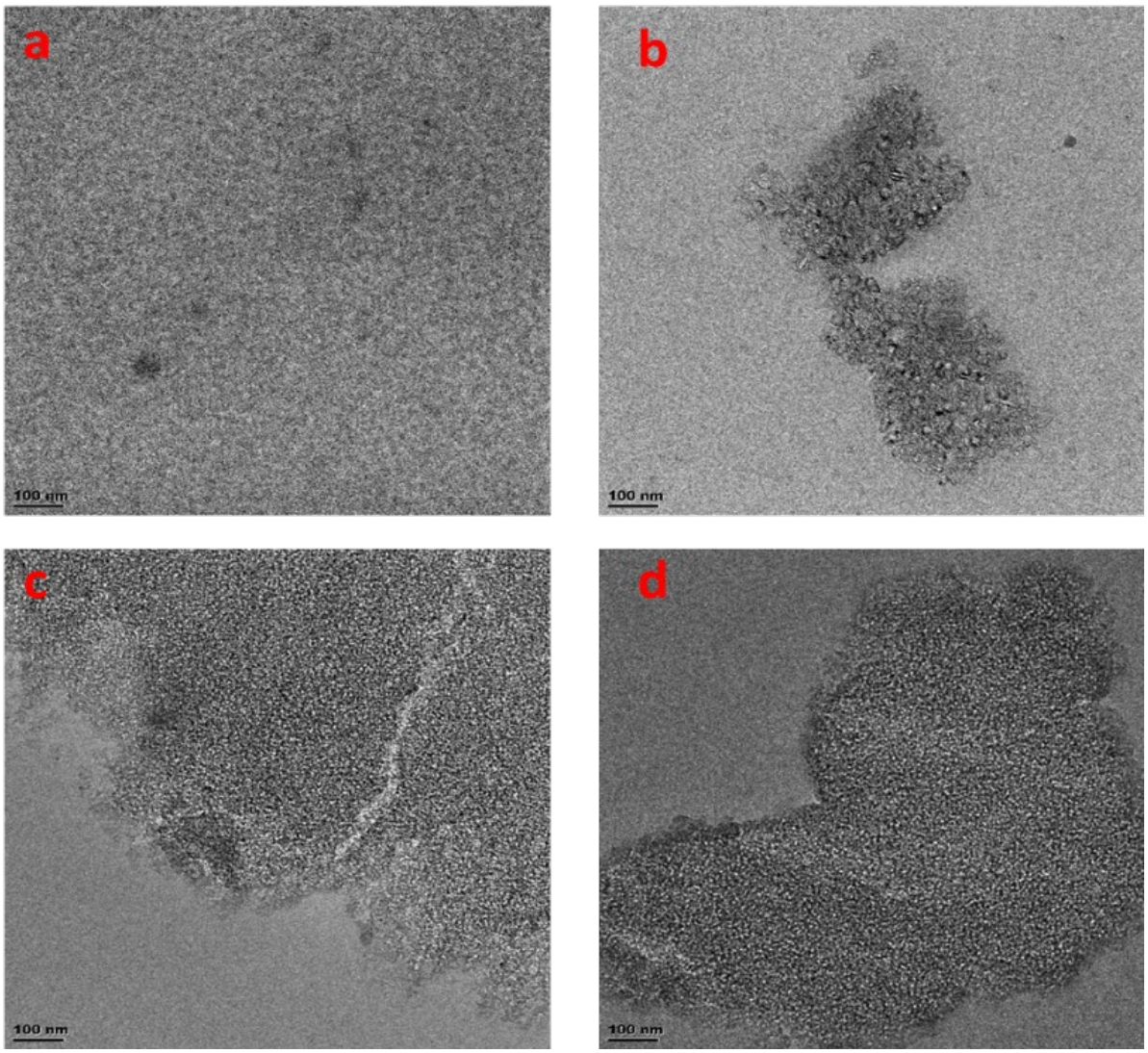

Fig. 5.3: TEM images of (a) PLA, PLA/SiO_2:0.4 mol% Sr^{2+}:x mol% Tb^{3+} composites (b) x = 0, (c) x = 0.1 and x = 0.5.

5.3.2 Thermal analysis

The effect of the phosphors on the thermal transitions of the PLA were studied with DSC, and Fig 5.4 shows the DSC heating curves of the samples. All samples exhibits three transitions, which are the glass transition (T_g) at about 60 ºC, cold crystallization (T_{cc}) at about 115 ºC and melting (T_m) at about 150 ºC, the observed values are not that different from those reported by other researchers [13]. There is a slight decrease in the T_g with the introduction of the phosphors into the PLA as shown in Fig 5.5. This decrease may be due to the plasticization of PLA by the

phosphors [25]. The composites show an increase in the T_{cc} as compared to PLA, while the T_m for all the samples do not show any significant difference. The observed increase in T_{cc} means that the filler restricted the crystallization of the polymer matrix. Table 5.2 depicts the exothermic and endothermic data of the PLA and composites as derived from Fig 5.4.

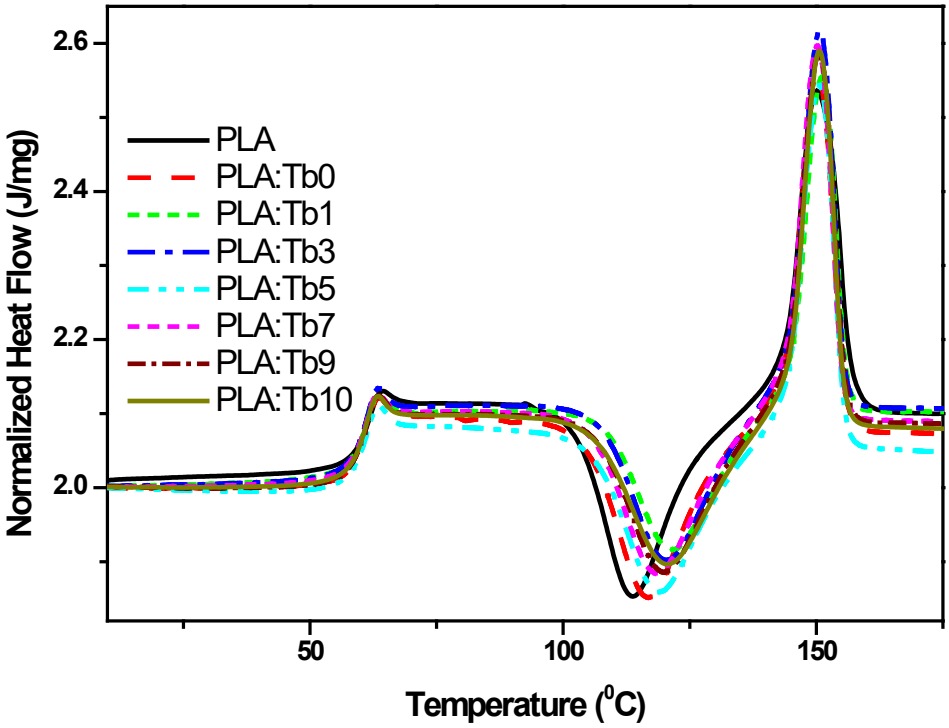

Fig. 5.4: DSC heating curves of PLA and composites.

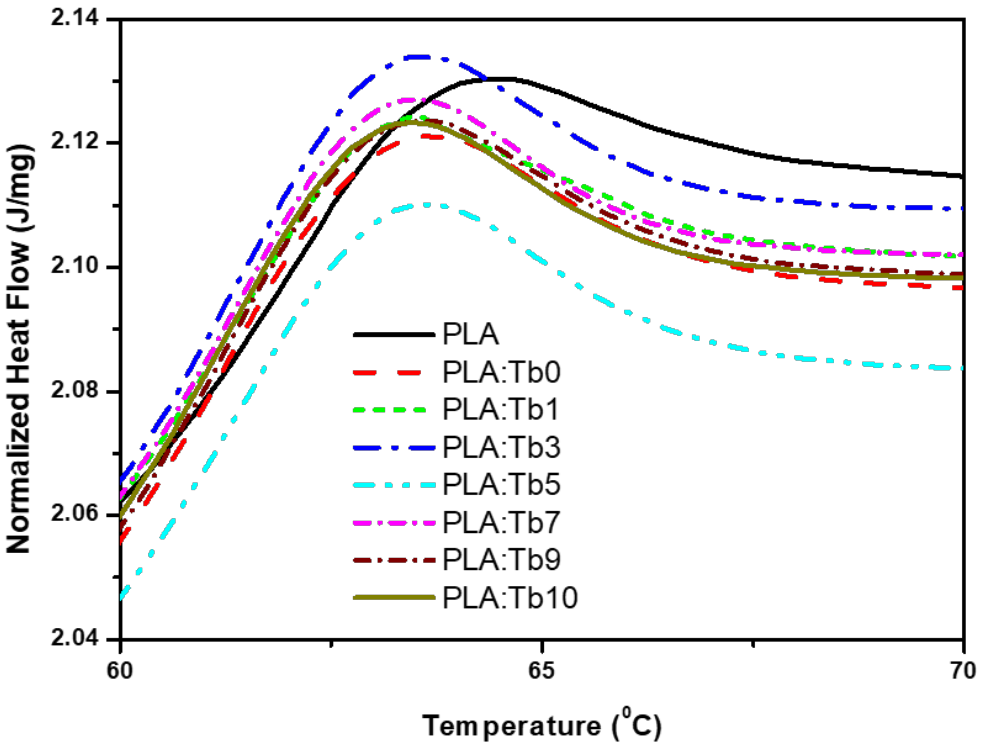

Fig. 5.5: Zoomed version of the DSC heating curves at 60 – 70 ºC.

Table 5.2: DSC heating data for the PLA and composites

	T_g (°C)	T_{cc} (°C)	T_m (°C)	ΔH_m (J g^{-1})
PLA	62.7 ± 0.14	112.9 ± 0.81	149.8 ± 0.63	26.3 ± 2.24
PLA:Tb0	62.4 ± 0.23	116.0 ± 0.23	149.8 ± 0.59	25.2 ± 0.53
PLA:Tb1	58.4 ± 0.11	120.5 ± 0.11	150.7 ± 0.45	24.0 ± 1.38
PLA:Tb3	62.5 ± 0.24	119.0 ± 0.49	150.1 ± 0.25	27.8 ± 4.06
PLA:Tb5	62.7 ± 0.19	117.9 ± 0.73	150.1 ± 0.25	23.3 ± 0.59
PLA:Tb7	62.5 ± 0.12	119.0 ± 0.24	150.4 ± 0.13	22.7 ± 0.63
PLA:Tb9	62.5 ± 0.10	119.1 ± 0.33	150.4 ± 0.11	23.6 ± 1.62
PLA:Tb10	55.7 ± 0.79	119.3 ± 0.49	150.5 ± 0.26	22.9 ± 1.10

*T_g is the glass transition temperature at the inflection point. T_m and T_{cc} are peak temperatures of melting and cold crystallization. While, ΔH_m enthalpy of melt.

Fig. 5.6 and 5.7 show the TGA and derivative thermogravimetric (DTG) curves of PLA and the PLA nanocomposites, which determine the thermal stability of the composites. The thermal degradation of all the samples experiences a one-stage weight loss. The incorporation of SiO_2 nanoparticles into the PLA polymer matrix does not have a significant impact on the thermal stability of the polymer, as shown in both Fig. 5.6 and 5.7. The onset temperature of thermal degradation of all the samples is approximately 310 °C, and the degradation completes at about 400 °C. Moreover, there was almost nothing left for all samples when the temperature increased above 500 ºC.

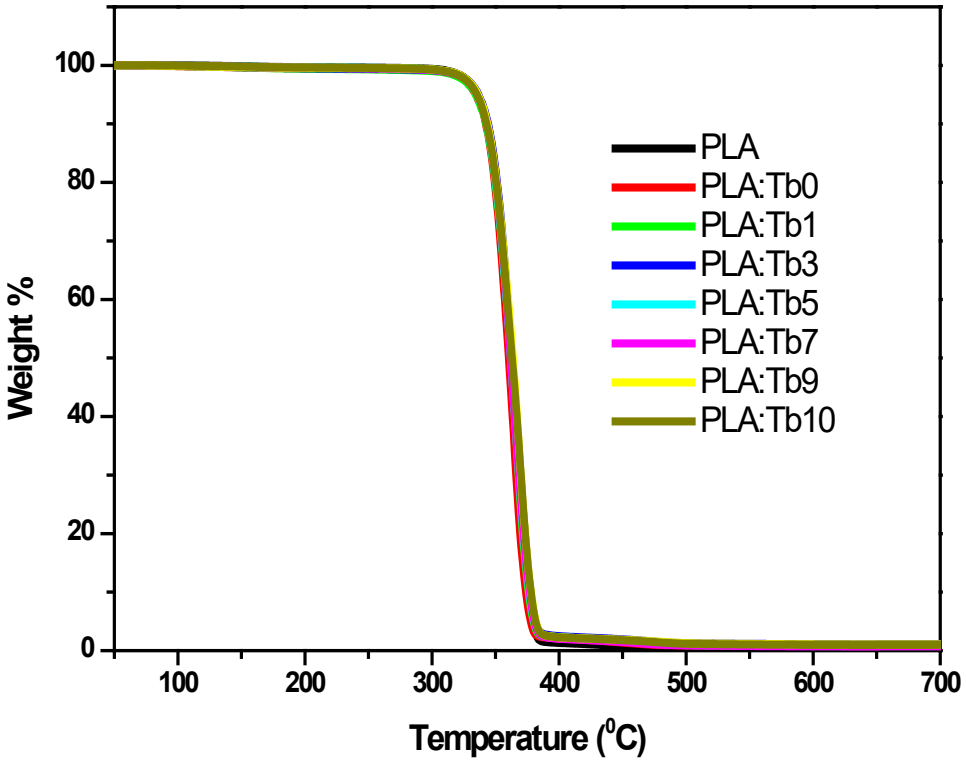

Fig. 5.6: TGA curves of PLA and PLA nanocomposites

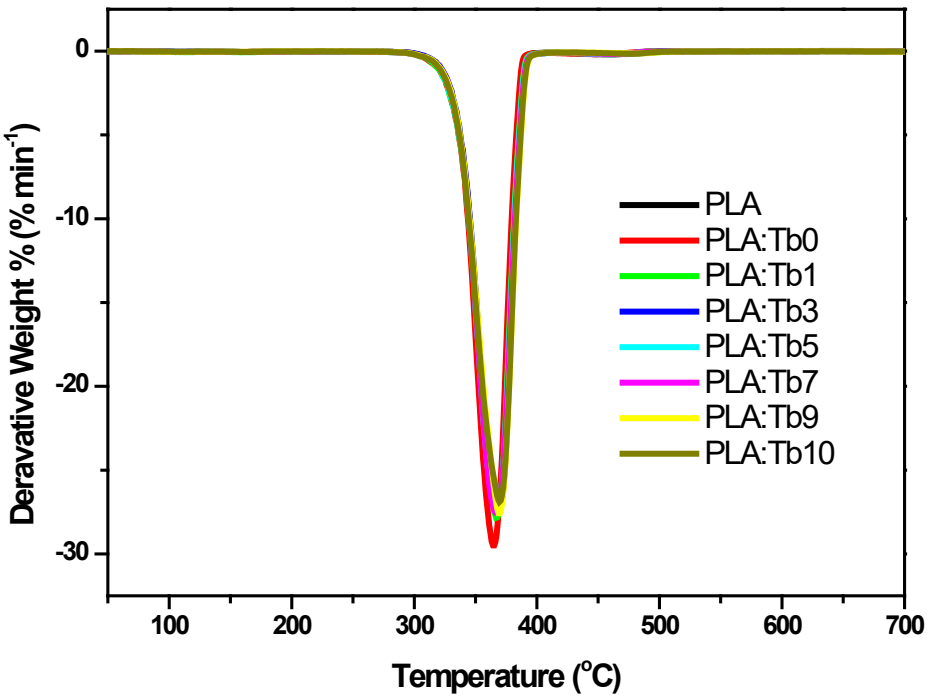

Fig. 5.7: DTG curves of PLA and PLA nanocomposites

5.3.3 Ultraviolet–visible (UV–vis) spectroscopy

The UV-vis measurements were done at room temperature in the spectral range from 300 - 800 nm. Fig. 5.8 illustrates the transmittance spectra of PLA and the composites. All the samples shows an absorption edge at around 340 nm. The introduction of the phosphors into the PLA matrix did not result in any shift of the absorption edge but rather reduced the transmittance of the polymer across the ultra-violet and visible range. The observed reduction in transmittance may be due to the agglomeration of the phosphors as shown by TEM results in Fig. 5.3. The observed behaviour of no shift to absorption edges with the introduction of the phosphors in PLA may be due to the agglomeration or inhomogenous distribution of the phosphor as seen in TEM analysis.

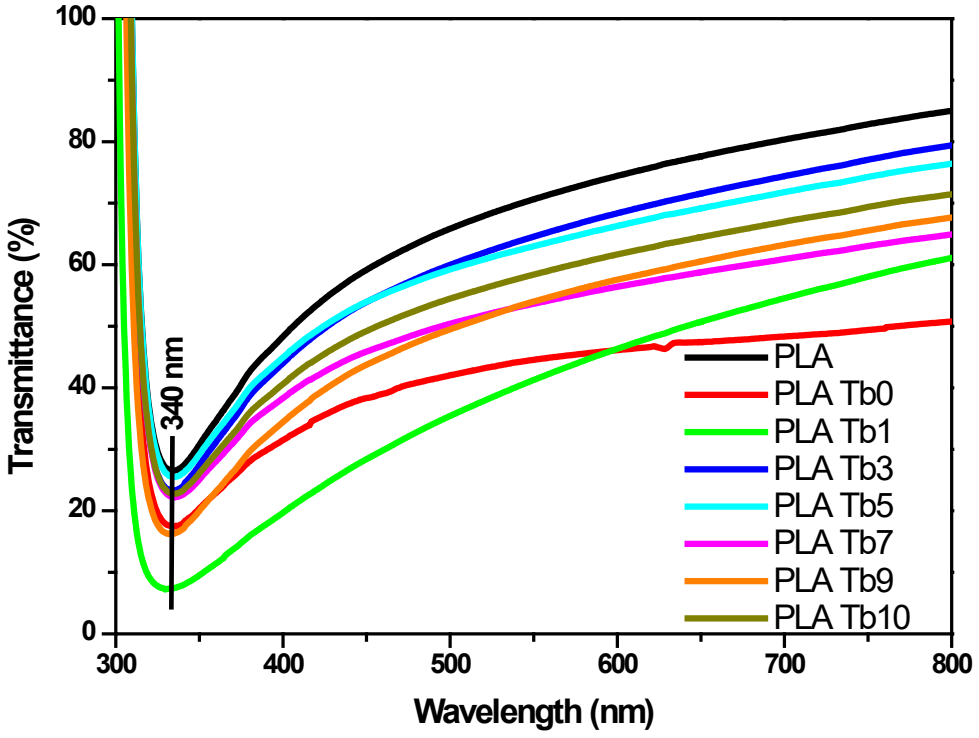

Fig. 5.8: UV-vis transmittance spectra of PLA and PLA/SiO_2:0.4mol%Sr^{2+}:x mol% Tb^{3+} (with $0 \leq x \leq 0.5$) composites.

5.3.4 Photoluminescence (PL)

The PL emission spectra of PLA and PLA/SiO_2:0.4mol% Sr^{2+}:x mol% Tb^{3+} (with $0 \leq x \leq 0.5$) composites excited with He–Cd laser at 325 nm in ambient temperature are shown in Fig. 5.9 (a) and Fig. 5.10. PLA and PLA/SiO_2:0.4 mol% Sr^{2+} composite exhibited asymmetric spectra with a maximum at about 412 nm and a shoulder band at around 440 nm. To understand better the properties of the PL emission spectrum of PLA in Fig. 5.9 (a) the multi-peak deconvolution of this band with the Gaussian fit function is shown in Fig. 5.9 (b). This result indicated that the broad asymmetric band for PLA emission is composed mainly of violet 3.27 eV (379 nm), blue 3.1 eV (400 nm), 3.0 eV (413 nm) and 2.82 eV (440 nm), and green 2.39 eV (519 nm)

bands. The source of these observed emission bands is due to $n \rightarrow \pi^*$ and $\pi \rightarrow \pi^*$ transition of pure PLA [25].

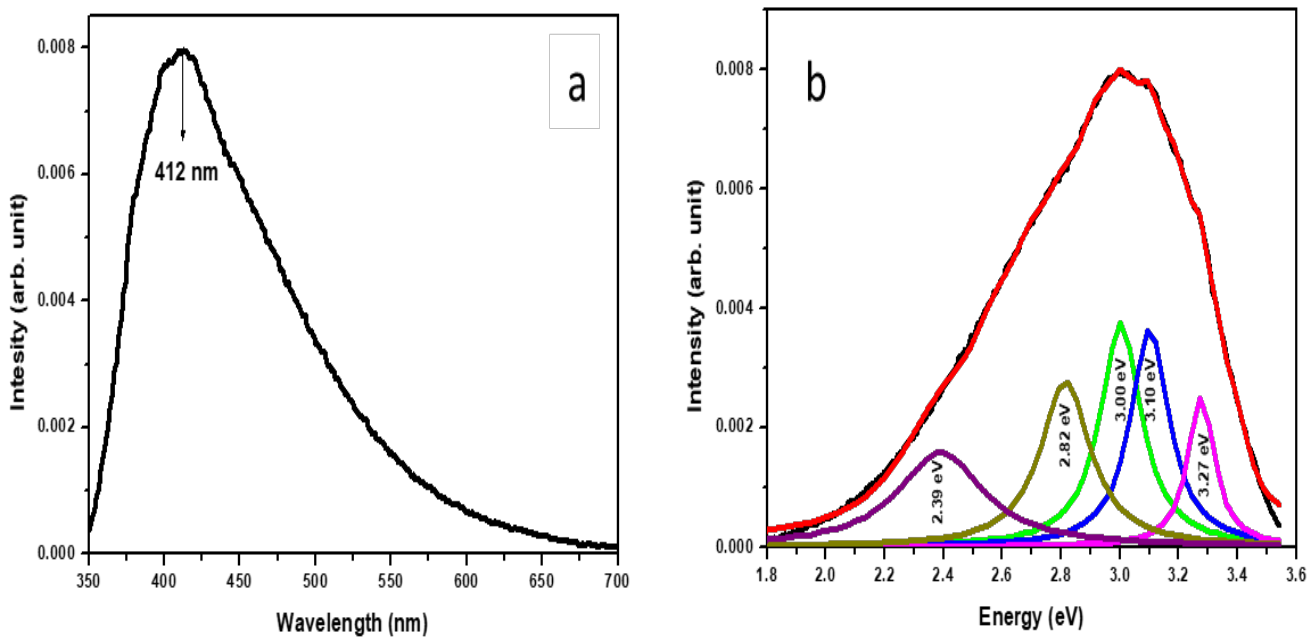

Fig. 5.9: The (a) emission and (b) deconvoluted spectrum of the PLA.

The PLA/SiO_2:0.4mol%Sr^{2+}:x mol% Tb^{3+} composites on the other hand exhibited asymmetric spectra with peaks at 412 nm, 487 nm, 543 nm, 582 nm and 621 nm. These peaks may be attributed to $^5D_3 - {}^7F_5$ and $^5D_4 - {}^7F_J$ (with J = 6, 5, 4, 3) transitions of Tb^{3+} [23, 26, 27].

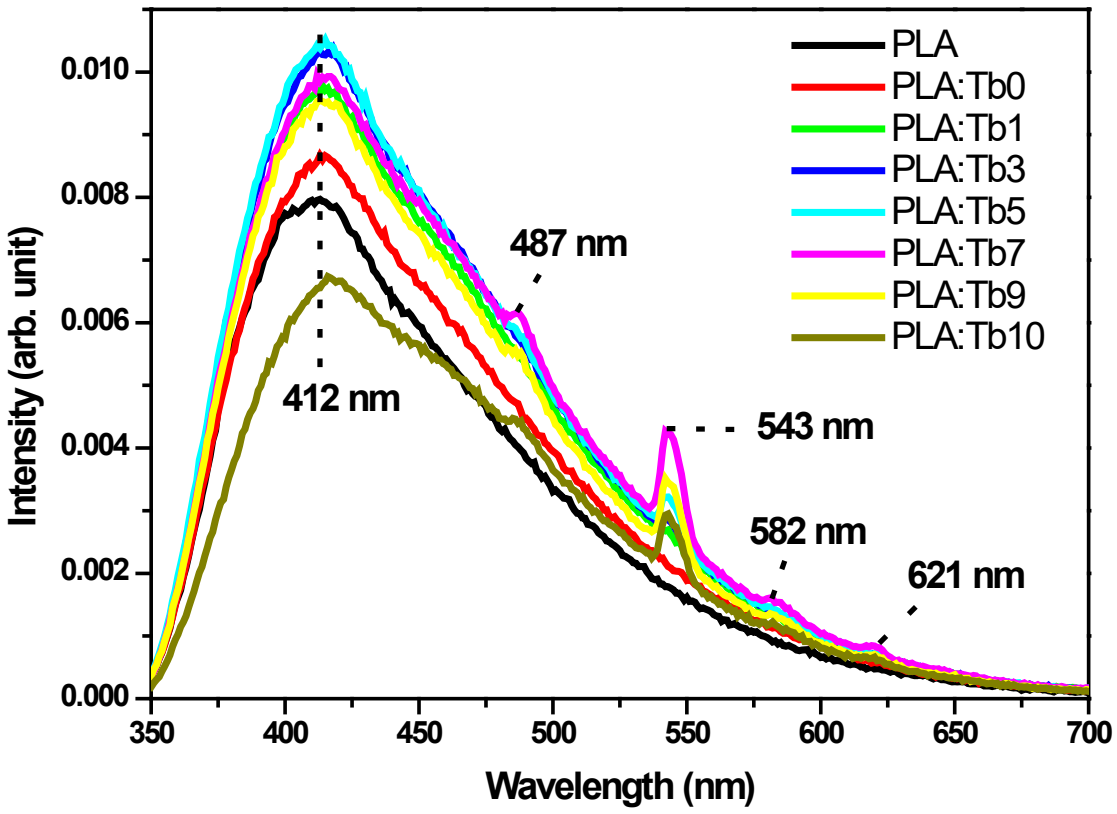

Fig. 5.10: PL emission spectra of PLA and PLA/SiO_2:0.4mol% Sr^{2+}:x mol% Tb^{3+} (with $0 \leq x \leq 0.5$) composites.

The emission intensity of the composites at 412 nm increased with the introduction of the phosphor into the PLA matrix and reached a maximum at Tb^{3+} concentration of 0.1 mol%, then showed a decrease at higher Tb^{3+} concentrations (see Fig. 5.11). The initial increase in intensity for the composites at 412 nm may be due to the improvement of SiO_2 defects emission. The peak at 543 nm increased in intensity up to x = 0.3 mol% Tb^{3+} and thereafter the intensity decreased as shown in Fig. 5.12. The observed decrease in intensity in Fig. 5.11 and Fig. 5.12 may be due to luminescence quenching mechanism as the Tb^{3+} ions concentration increases [22]. Fig. 5.13 illustrates the proposed luminescence mechanism based on the observed luminescence emissions as shown in Fig. 5.9 and Fig. 5.10.

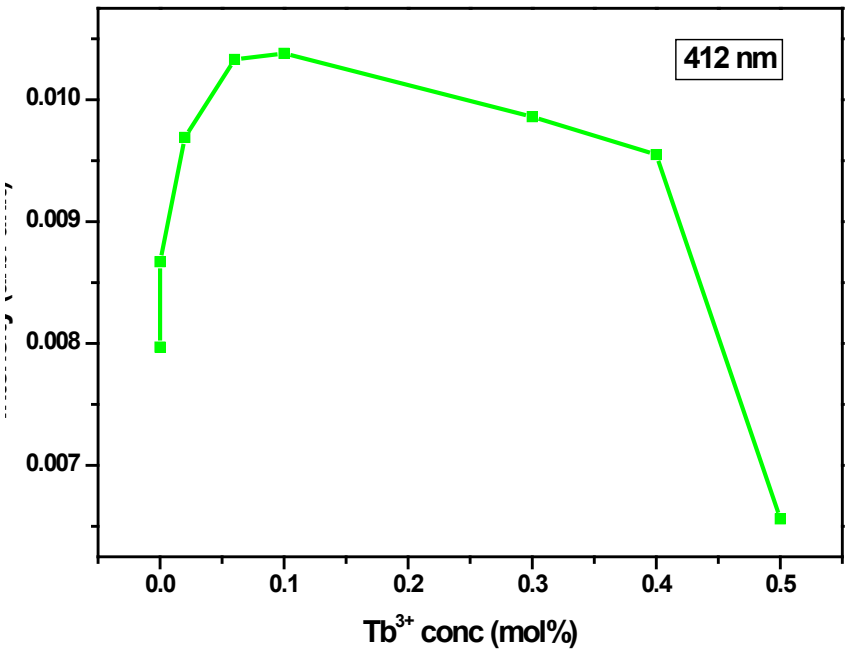

Fig. 5.11: PL intensity as a function of Tb^{3+} concentration at 512 nm

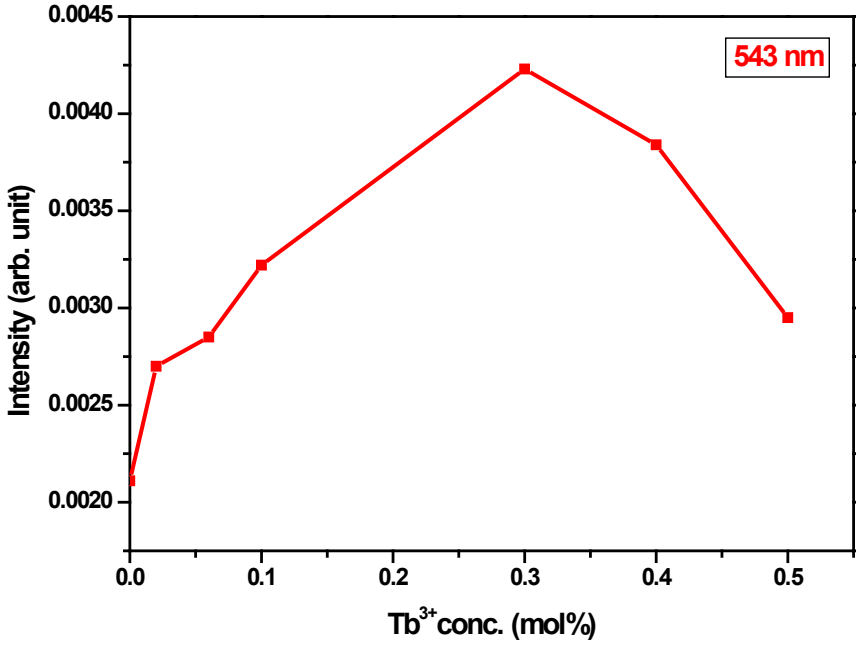

Fig. 5.12: PL intensity as a function of Tb^{3+} concentration at 543 nm

Fig 5.13 shows the emission pathways of PLA and its composites, as depicted by the PL results above. The observed emissions are from the PLA (and may be ascribed to the defects within the polymer matrix) and the d-f transitions of Tb^{3+}.

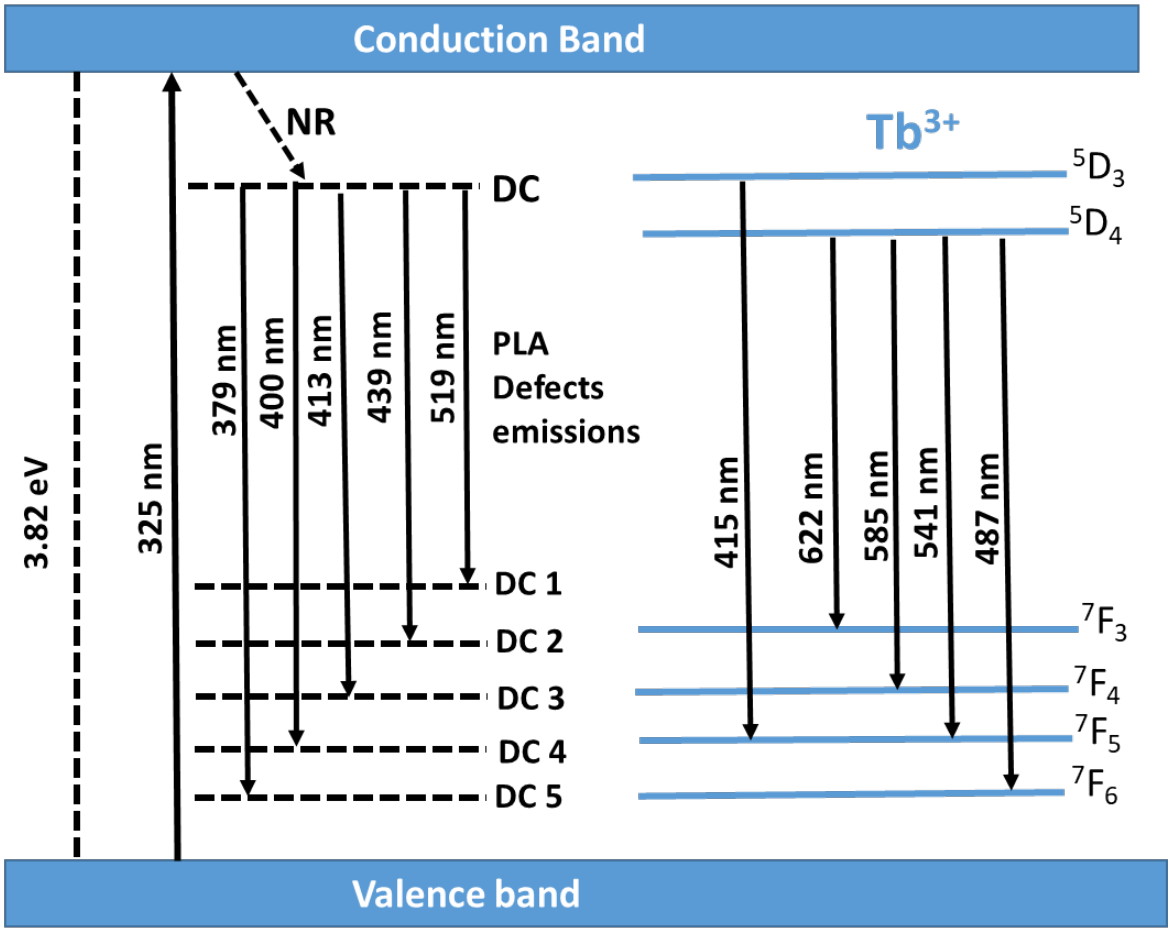

Fig. 5.13: The proposed emission pathways for PLA and PLA/SiO_2:0.4 mol% Sr^{2+}:x mol% Tb^{3+} (with $0 \leq x \leq 0.5$) composites.

Fig. 5.14 shows the Commission Internationale de l'Éclairage (CIE) chromaticity diagram of PLA and composites when excited at the wavelength of 325 nm. The CIE chromaticity diagram display the position of the coordinates and the expected colour of the samples. The colour of the PLA and composites were found in the blue vertex, which, suggests that the incorporation of the phosphors into PLA does not significantly influence the emission colour. This may be due to the distribution of the phosphors in PLA matrix not being homogenous as observed in the TEM images.

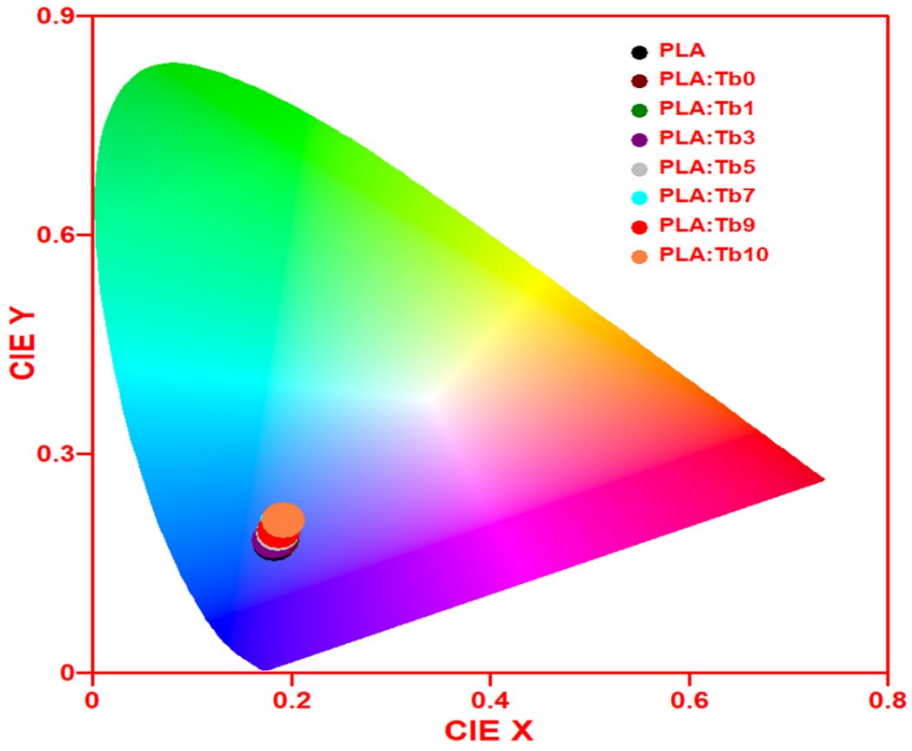

Fig. 5.14: CIE chromaticity diagram of PLA and PLA/SiO_2:0.4 mol% Sr^{2+}:x mol% Tb^{3+} (with $0 \leq x \leq 0.5$) composites.

5.4 Conclusion

Nanocomposites of SiO_2:0.4mol% Sr^{2+}:x mol% Tb^{3+} (with x = 0.02, 0.06, 0.1, 0.3, 0.4, 0.5) nano-powders dispersed in PLA polymer matrix were successfully prepared through melt mixing. The XRD results showed broad peaks for all samples, which meant the samples were amorphous. The challenge as shown by the TEM images is that the filler particles tend to agglomerate in the polymer matrix. The introduction of the nano-powders into the polymer matrix did not result in the change in the morphology of the PLA matrix. From the DSC results, it was observed that the composites had increased the T_{cc} and slightly decreased the T_g as compared to PLA. While the introduction of the phosphor particles did not have a significant impact on the thermal stability of PLA as shown by TGA. From the UV results, it was observed that the introduction of the phosphor only affected the transmittance of the polymer matrix. The emission peaks that can be associated with the Tb^{3+} transitions were observed with the

dispersion of the nano-powders into the PLA. The CIE showed that the colour for all the samples was in the blue vertex.

References

1. R. Piramidowicz, A. Jusza, L. Lipinska, M. Gil, P. Mergo, *Opt. Mater*. 87 (2019) 35 -41.

2. Ž. Antic, R. Krsmanovic, M. Marinovic-Cincovic, M.D. Dramicanin, *Acta Physica PolonicaA* 117(5) (2010) 831 – 836.

3. A. G. Bispo-Jr, N. A. Oliveira, C. X. Cardoso, S. A. M. Lima, A. E. Joba, I. O. Osorio Romána, C. S. Danna, A. M. Pires, *Mater. Chem. Phys.* 217 (2018) 160 -167.

4. J. Prakash, V. Kumar, L. J. B. Erasmus, M. M. Duvenhage, G. Sathiyan, S. Bellucci, S. Sun, H. C. Swart, *ACS Appl. Nano Mater.* 1 (2018) 977−988.

5. A. Potdevin, G. Chadeyron, S. Therias, R. Mahiou, *Langmui*r 28 (2012) 13526 – 13535.

6. J.P. Zou, P. Le Rendu, I. Musa, S.H. Yang, Y. Dan, C.T. That, T.P. Nguyen, *Thin Solid Films* 519(12) (2011) 3997 – 4003.

7. A. Mayolet, W. Zhang, E. Simoni, J.C. Krupa, P. Martin, *Opt. Mater.* 4(6) (1995) 757 - 769.

8. X. Zhu, P. Lu, W. Chen, J. Dong, *Polymer*, 51(14) (2010) 3054 – 3063.

9. S. B. Mishra, A. K. Mishra, N. Revaprasadu, K. T. Hillie, W. J. vd M. Steyn,

E. Coetsee, H. C. Swart, *J. App. Polym. Sci.* 112 (2009) 3347–3354.

10. T. Rimpongpisarn, W. Wattanathana, K. Sukthavorn, N. Nootsuwan, Y. Hanlumyuang, C. Veranitisagul, A. Laobuthee, *Mater. Lett.* 237 (2019) 270-273.

11. B.W. Chieng, N. A. Ibrahim, W. Md Zin Wan Yunus, M. Z. Hussein, Y.Y. Then, Y.Y. Loo, *Polymers 6* (2014) 2232-2246.

12. M. Gong, Q. Zhao, L. Dai, Y. Li, T. Jiang, *J. Asian Ceram. Soc.* 5 (2017) 160–168.

13. B.W. Chieng, N.A. Ibrahim, W. Md Zin Wan Yunus, M.Z. Hussein, *Sci. Res. J.* 11(2) (2014) 1 – 13.

14. X. Wen, K. Zhang, Y. Wang, L. Han, C. Han, H. Zhang, S. Chen, L. Donga, *Polym. Int.* 60 (2011) 202–210.

15. Jean-Marie Raquez, Y. Habibi, M. Murariu, P. Dubois, *Prog. in Polym. Sci.* 38 (2013) 1504– 1542.

16. H. Zou, S. Wu, J. Shen, *Chem. Rev.* 108 (2008) 3893–957.

17. S. Yan, J. Yin, Y. Yang, Z. Dai, J. Ma, X. Chen, *Polym.* 48 (2007)1688–1694.

18. L. Wu, D. Cao, Y. Huang, B. Li, *Polym.* 49 (2008) 742–748.

19. J. Zhang, J. Lou, S. Ilias, P. Krishnamachari, J. Yan, *Polym.* 49 (2008) 2381–2386.

20. S.V. Motloung, F.B. Dejene, H.C. Swart, O.M. Ntwaeaborwa, *Ceram. Int.* 41 (2015) 6776–6783.

21. L.F. Koao, H.C. Swart, E. Coetsee, M.M. Biggs, F.B. Dejene, *Physica B* 404 (22) (2009) 4499–4503.

22. R.G. Moji, R.E. Kroon, S.V. Motloung, T.E. Motaung, I. Ahemen, L.F. Koao, *Mater. Chem. Phys.* 242 (2020) 122409.

23. R.G. Moji, R.E. Kroon, S.V. Motloung, T.E. Motaung, L.F. Koao, *Physica B: Phys. Cond. Matter 580 (2020) 411817.*

24. J.P. Mofokeng, A.S. Luyt, Polymer Testing 45 (2015) 93 -100 25. L. Klapiszewski, F. Pawlak, J. Tomaszewska, T. Jesionowski, *J. Polym.* 7 (2015) 1767-1788.

25. K. K. Gupta, P.K. Mishra, P. Srivastava, M. Gangwar, G. Nath, P. Maiti, App. Surface Sci. 264 (2013) 375–382.

26. O.M. Ntwaeaborwa, H.C. Swart, R.E. Kroon, P.H. Holloway, J.R. Botha, *J. Phys. Chem. Solids* 67 (2006) 1749–1753, https://doi.org/10.1016/j.jpcs.2006.04.002.

27. L.F. Koao, B.F. Dejene, H.C. Swart, S.V. Motloung, T.E. Motaung, S.P. Hlangothi, *Adv. Mater. Lett.* 7 (7) (2016) 529-535.

Chapter 6 – Conclusion and future work

6.1 Conclusion

The aim of this work is to study the morphological, optical and luminescence properties of the SiO_2, SiO_2 singly doped (with Sr^{2+}) and SiO_2:Sr^{2+} co-doped (with Tb^{3+}) phosphors immobilized into the PLA matrix. The sol-gel technique was used to successfully prepare the phosphor samples. The XRD showed that the singly doped samples changed from amorphous (SiO_2) to crystalline state with the increase in Sr^{2+} concentration, while the co-doped samples were found to be amorphous. EDS confirmed the presence of expected elements in all the samples. The SEM images for the singly doped samples show irregular agglomerated particles, with no apparent difference in size with increasing Sr^{2+} concentration. While the SEM images for co-doped samples show agglomerated spherical nanoparticles. The TEM results support the observation from the XRD as well as SEM for singly doped and co-doped samples.

The UV spectra shows that the absorption edge at around 400 nm (from the host) shifts to around 365 nm for both the singly doped and co-doped samples. The observed shift of absorption edge to lower wavelength may be due the alteration of the defects induced by the dopants. The PL results show that the SiO_2 has a broad emission peak with a maximum at around 415 nm. It clear that the Sr^{2+}- doped and Tb^{3+}-co-doped have effect on both luminescence intensity and wavelength compared to undoped SiO_2. It was noted that the incorporation of Sr^{2+} into SiO_2 could promote the formation of more defects in the SiO_2 lattice due to difference in the valence states of Sr^{2+} and Si^{4+}. The CIE analysis showed that the colour coordinates for the x = 0.2 and 0.4 mol% Sr^{2+} well related to white light emission, while varying the Sr^{2+} concentration influenced the emission colour shift. The PL emission spectra for the co-doped samples showed emission peaks from both the SiO_2 and Tb^{3+}, with energy

transfer being proposed from the SiO_2 to Tb^{3+}. The addition of Tb^{3+} in co-doped samples tuned the colour of the phosphors from blue to green as shown by the CIE colour chromaticity.

Nanocomposites of SiO_2:0.4 mol% Sr^{2+}:x mol% Tb^{3+} (with x = 0.02, 0.06, 0.1, 0.3, 0.4, 0.5) nano-powders dispersed in PLA polymer matrix were successfully prepared through melt mixing. The challenge as shown by the TEM images is that the filler particles tend to agglomerate in the polymer matrix. The XRD results showed broad peaks for all samples, which meant the samples were amorphous. The introduction of the nano-powders into the polymer matrix did not result in the change in the morphology of the samples. As far as the thermal properties are concerned, the phosphor particles increased the T_{cc} but did not have significant impact on the thermal stability. From the UV results, it was observed that the introduction of the phosphor only affected the transmittance of the polymer matrix. The emission peaks that can be associated with the Tb^{3+} transitions were observed with the dispersion of the nano-powders into the PLA. The CIE showed that the colour for all the samples was in the blue vertex.

6.2 Future work

The following areas are proposed for future work:

- Comparison of the annealed and un-annealed phosphor samples.
- The possible use of a compatibilizer to address the challenge as shown by the TEM images is that the filler particles tend to agglomerate in the polymer matrix and its effect on the luminescence.
- This difference in diffraction pattern between the composites and PLA needs further investigation.

- The possible introduction of a substance that will make the PLA less brittle thus allowing it to be available for more applications.
- It could be interesting to study the effect of using higher filler concentrations on the luminescence of the composites.

Conferences and Publications

Conferences

1. R.G. Moji, L.F. Koao, J.P. Mofokeng, R.E. Kroon, S.V. Motloung, T.E. Motaung. Morphology, structural and luminescent properties of sol-gel synthesized SiO_2:0.4 mol% Sr^{2+}: x mol% Tb^{3+}nanopowders. 8th South African Conference on Photonic Materials, 06 -10 May 2019, Kariega Game Reserve, South Africa.

Publications

1. R.G. Moji, R.E. Kroon, S.V. Motloung, T.E. Motaung, I. Ahemen, L.F. Koao, Colour tuning and white light emission from sol-gel SiO_2 nanoparticles doped with Sr^{2+}. *Materials Chemistry and Physics* 242 (2020) 122409.
2. R.G. Moji, R.E. Kroon, S.V. Motloung, T.E. Motaung, L.F. Koao, Morphology, structural and luminescent properties of sol-gel synthesized SiO_2 powders co-doped with Sr^{2+} and Tb^{3+}. *Physica B: Condensed Matter,* 580 (2020) 411817.

Papers under preparation

1. Characterization of SiO_2 co-doped with Sr^{2+} and Tb^{3+} phosphors immobilized in PLA.